ISTANBUL TECHNICAL UNIVERSITY ★ INSTITUTE OF SCIENCE AND TECHNOLOGY

NOVEL ANALYTICAL CONTINUATION BASED SHAPE RECONSTRUCTION METHODS FOR PERFECT ELECTRIC CONDUCTING TARGETS

Ph.D. Thesis by
Mehmet ÇAYÖREN

Department : **Electronics and Communications Engineering**

Programme : **Telecommunications Engineering**

JUNE 2009

ISTANBUL TECHNICAL UNIVERSITY ★ INSTITUTE OF SCIENCE AND TECHNOLOGY

NOVEL ANALYTICAL CONTINUATION BASED SHAPE RECONSTRUCTION METHODS FOR PERFECT ELECTRIC CONDUCTING TARGETS

Ph.D. Thesis by
Mehmet ÇAYÖREN
(504042308)

Date of submission	:	**27 February 2009**
Date of defence examination	:	**10 June 2009**

Supervisor (Chairman)	:	**Prof. Dr. İbrahim AKDUMAN (ITU)**
Members of the Examining Committee		**Prof. Dr. İrşadi AKSUN (Koc U.)**
		Prof. Dr. Mevlüt TEYMÜR (ITU)
		Assoc. Prof. Dr. Ali YAPAR (ITU)
		Assoc. Prof. Dr. İbrahim TEKİN (Sabanci U.)

JUNE 2009

MÜKEMMEL ELEKTRİK İLETEN HEDEFLER İÇİN
ANALİTİK DEVAM TEMELLİ YENİ ŞEKİL BELİRLEME YÖNTEMLERİ

DOKTORA TEZİ
Mehmet ÇAYÖREN
(504042308)

Tezin Enstitüye Verildiği Tarih　:　**27 Şubat 2009**

Tezin Savunulduğu Tarih　:　**10 Haziran 2009**

Tez Danışmanı　:　**Prof. Dr. İbrahim AKDUMAN (İTÜ)**
Diğer Jüri Üyeleri　　**Prof. Dr. İrşadi AKSUN (Koç Ü.)**
　　　　　　　　Prof. Dr. Mevlüt TEYMÜR (İTÜ)
　　　　　　　　Doç. Dr. Ali YAPAR (İTÜ)
　　　　　　　　Doç. Dr. İbrahim TEKİN (Sabancı Ü.)

HAZİRAN 2009

FOREWORD

Foremost, I would like to express my sincere gratitude to my thesis supervisor, Prof. Dr. İbrahim Akduman, for his guidance and support during my PhD studies. He has been an inspiring advisor who profoundly influenced my research.

I would like to express my appreciation to Assoc. Prof. Dr. Ali Yapar for his valuable contributions and guidance.

During my studies, I had the opportunity to collaborate with several researchers. Particular thanks are given to Dr. Lorenzo Crocco, Prof. Dr. Fioralba Cakoni, Prof. Dr. David Colton and Prof. Dr. Sungkwon Kang whom affected my research either directly or indirectly.

I would like to thank to members of Electromagnetic Research Group (ERG) for the great environment. Also I would like to thank to Dr. Serkan Şimşek and Dr. Fatih Yaman for their long-standing friendship.

I would like to acknowledge the Scientific and Technological Research Council of Turkey (TÜBİTAK) for both awarding me with a Ph.D. scholarship and for providing financial support during my 9-months visit in Mathematical Sciences Department of University of Delaware.

Finally, I would like to thank my family for their continuous support. My mother Zeynep, my father Seyfettin and my brothers Cemal and Hüseyin constantly encouraged me and this thesis is dedicated to them.

June 2009   Mehmet ÇAYÖREN

TABLE OF CONTENTS

ABBREVIATIONS

2D	:	Two dimensional
IBC	:	Impedance boundary condition
PEC	:	Perfect electric conductor
SIBC	:	Standard impedance boundary condition
SNR	:	Signal to noise ratio
SVD	:	Singular value decomposition
TSVD	:	Truncated singular value decomposition

x

LIST OF TABLES

LIST OF FIGURES

LIST OF SYMBOLS

A^*	:	Adjoint of an operator A
A^T	:	Transpose of matrix A
D	:	Cross section of the scatterer
$\mathbf{E}$	:	Electric field vector
$G(\mathbf{x}, \mathbf{y})$	:	Green's function for Helmholtz equation
$\mathbf{H}$	:	Magnetic field vector
J_F	:	Jacobian of operator F
L	:	Number of points sampled on the boundary of the object
M	:	Upper bound of Taylor series
N	:	Number of measurements
P	:	Least square regularization parameter
R	:	Regularization parameter
S	:	Far field operator
T	:	Number of measurement points
$Z(\mathbf{x})$	:	Inhomogeneous surface impedance
Z_0	:	Intrinsic impedance of background medium
k	:	Wavenumber
$u^\infty(\hat{\mathbf{x}})$	:	Far field pattern
$u^i(\mathbf{x})$	:	Incident field
$u(\mathbf{x})$	:	Total field
$u^s(\mathbf{x})$	:	Scattered field
$\mathbf{x}, \mathbf{y}$	:	Location vectors
x_1, x_2	:	Cartesian coordinates
α	:	Radius of the minimum circle covering the target
β	:	Radius of the circle where Taylor series expansion is applied
θ_n	:	Incidence angle for n-th illumination
μ	:	Permeability of the background medium
$\eta(\phi)$	:	Normalized surface impedance
ε	:	Permittivity of the background medium
λ	:	Wavelength
ϕ, τ	:	Angular variables
σ	:	Conductivity of the background medium
σ_v	:	v-th singular value
$\psi(\mathbf{x})$	:	Single layer potential density
$\varphi(\mathbf{x})$	:	Double layer potential density
∂D	:	Boundary of the scatterer
γ	:	Radius of the impedance circle
$f(\phi)$	:	Parametric representation of unknown surface
$\hat{f}(\phi)$	:	Estimate of $f(\phi)$
$H_v^{(1)}(.)$	:	First kind of Hankel function of v-th order
Δ	:	Laplace operator

$\hat{\mathbf{n}}, n(\mathbf{y})$: Outward surface normal
ω : Radial frequency
$\langle, \rangle$: Inner product
$||.||$: Euclidean norm of the operator
$\delta(.)$: Dirac delta function
C : Euler-Mascheroni constant
ξ : Noise ratio

NOVEL ANALYTICAL CONTINUATION BASED SHAPE RECONSTRUCTION METHODS FOR PERFECT ELECTRIC CONDUCTING TARGETS

SUMMARY

In this thesis, the inverse scattering problem of which the aim is to remotely retrieve the shape of an inaccessible, perfect electric conducting target through the use of electromagnetic waves is studied. This is one of the fundamental questions in inverse scattering theory and from the theoretical perspective; it is a nonlinear ill-posed problem. Thus the existence and the uniqueness of a stable solution cannot be anticipated initially. Within this framework, two new shape reconstruction methods are developed in this thesis. These methods can be classified as analytical continuation (or decomposition) methods in which the nonlinearity and the ill-posedness of the underlying problem are handled separately.

The first method is based on the analytical continuation of the scattered field by means of Taylor series expansion. In particular, the measured far-field data which is corrupted with inevitable measurement noise first backpropagated to a circular domain enclosing the inaccessible object in terms of regularized inversion of a single layer potential. The reconstructed single layer potential density enables to approximate scattered field outside of the encircled object quite accurately, while a Taylor series expansion in the radial direction is exploited to represent the field in the vicinity of the target. From the boundary condition, the problem is then recast as a polynomial equation containing the contour of the object as an unknown. Later this nonlinear equation is iteratively solved via the Gauss-Newton algorithm to retrieve the unknown shape.

The second method introduced in this thesis is based on creating an equivalent scattering problem by means of standard impedance boundary condition (SIBC). More precisely, the inaccessible perfectly conducting target is modeled as a circular impedance cylinder having inhomogeneous surface impedance. By virtue of equivalence, the impedance cylinder generates the same field distribution on whole space outside of the inaccessible object, as long as the latter is enclosed by the inaccessible target. In order to determine the equivalent surface impedance, first the measured far-field data which is corrupted with noise is backpropagated to the surface of the impedance cylinder, through the regularized inversion of the single-layer potential. Then, the surface impedance is recovered by exploiting the SIBC imposed over the impedance cylinder. Since the reconstructed surface impedance enables to represent scattered field outside of the unknown target, the retrieval of the unknown shape turns out to be the solution of a nonlinear optimization problem, which is solved iteratively through the Gauss-Newton algorithm.

Several numerical simulations are performed to validate and to expose both capabilities and the limitations of the presented methods. As a result, it is concluded that both methods provide quite accurate reconstructions for the objects having starlike boundaries with both convex and concave parts. It is observed that the size of the object should be comparable to the wavelength when only a single illumination is

employed. However this limitation can be overcome in multiview configuration where several plane waves with different incidence directions are employed. Moreover the multiview data improves the robustness against to noise such that it becomes possible to reconstruct with lower signal-to-noise ratios (SNR).

MÜKEMMEL ELEKTRİK İLETEN HEDEFLER İÇİN ANALİTİK DEVAM TEMELLİ YENİ ŞEKİL BELİRLEME YÖNTEMLERİ

ÖZET

Bu tez çalışması kapsamında yanına erişilemeyen, mükemmel elektrik ileten cisimlerin elektromagnetik dalgalar aracılığıyla şekillerinin uzaktan belirlenmesi konulu ters saçılma problemi incelenmiştir. Bu konu ters saçılma teorisindeki temel sorulardan biridir ve teorik açıdan doğrusal olmayan, kötü kurulmuş bir problemdir. Bu nedenle baştan kararlı bir çözümün varlığı ve tekliği öngörülemez. Bu çerçevede, bu tez çalısmasında iki adet yeni şekil belirleme yöntemi geliştirilmiştir. Bu yöntemler problemin doğrusal olmayan ve kötü kurulmuş parçalarının ayrı ayrı kotarıldığı analitik devam (veya ayrıştırma) yöntemleri olarak sınıflandırılabilirler.

Geliştirilen ilk yöntem saçılan alanın Taylor serisi açılımıyla analitik olarak devamına dayanmaktadır. Ölçüm gürültüsüyle bozulmuş olan uzak alan verisi öncelikle cismi çevreleyen dairesel bir bölgeye, bir tek-katman potansiyelinin regülerize edilmiş biçimde tersi alınarak devam ettirilir. Elde edilen bu tek-katman potansiyel yoğunluğu erişilemeyen cisim dışındaki bölgede alanı yeterince iyi biçimde ifade etmeye olanak verirken, Taylor serisi açılımı radyal dogrultuda içe doğru olan bölgede alanı ifade etmek için kullanılmıştır. Cismin üzerindeki sınır koşulu yardımıyla, problem cismin sınırının bilinmeyen olarak gözüktüğü polinom yapısındaki bir eşitliğe dönüştürülür. Ardından bu doğrusal olmayan eşitlik Gauss-Newton algoritması aracılığıyla yinelemeli olarak çözülerek, bilinmeyen şekil belirlenir.

Geliştirilen ikinci yöntemse standart empedans sınır koşulu (SIBC) anlamında eşdeğer bir saçılma probleminin oluşturulmasına dayanmaktadır. Daha ayrıntılı belirtmek gerekirse, yanına erişilemeyen iletken hedef, üzerinde homojen olmayan bir yüzey empedansına sahip dairesel bir empedans silindiri olarak modellenir. Eşdeğer problem anlamında, empedans silindiri cismin içinde kaldığı sürece, yanına erişilemeyen cismin dışındaki bölgede cisimle aynı alan dağılımı yaratacaktır. Eşdeğer yüzey empedansının belirlenmesi için, ilk yöntemdekine benzer olarak gürültülü uzak alan verisi, bir tek-katman potansiyelinin regülerize edilmiş tersi aracılığıyla empedans silindirinin yüzeyine kadar devam ettirilir. Ardından, yüzey empedansı empedans silindiri üzerinde tanımlanan SIBC kullanılarak bulunur. Bulunan bu yüzey empedansı cismin dışındaki bölgede alanı ifade etmeye imkan verdiğinden cismin yüzeyindeki sınır koşulu yardımıyla, bilinmeyen yüzeyin bulunması problemi Gauss-Newton algoritmasıyla yinelemeli olarak çözülen doğrusal olmayan bir optimizasyon problemine dönüştürülür.

Tanıtılan yöntemleri hem sayısal olarak doğrulamak hem de yöntemlerin sınırlamalarını ortaya çıkarmak amacıyla çesitli simülasyonlar gerçekleştirilmiştir. Sonuç olarak, her iki metodunda hem konveks hem de konkav tarafları olan yıldız-biçimi sınıra sahip cisimler için oldukça iyi sonuçlar verdiği sonucuna varılmıştır. Tek bir aydınlatmanın kullanılması durumunda cismin boyutlarının dalgaboyu mertebesinde olması gerektiği gözlemlenmiştir. Öte yandan bu sınırlama,

farklı geliş açılarına sahip birden çok düzlem dalganın kullanıldığı çoklu aydınlatma kullanımıyla aşılabilmektedir. Dahası çoklu aydınlatma kullanımı gürültüye olan duyarlılığı iyileştirerek daha düşük işaret-gürültü-oranlarında da şekillerin belirlenebilmesine olanak vermektedir.

1. INTRODUCTION

The inverse scattering problems are encountered in many areas of engineering and applied sciences such as medical imaging, microwave remote sensing, geophysical exploration, or non-destructive testing, etc. In these inverse problems, the basic aim is to identify the desired features of inaccessible objects (or mediums) remotely, through the use of electromagnetic, acoustical or elastic waves, depending on the physical requirements of the applications. The scattered wave which is the result of the interaction between the obstacles and the incident wave is exploited in order to extract physical and geometrical properties of the scatterers such as shape, location or electrical constitutive parameters.

The material properties of the objects to be reconstructed mainly determine the solution approaches of the related inverse scattering problems. If the object is impenetrable such as sound soft targets for acoustical case and perfect electric conductors for the electromagnetic case etc.; the problem becomes a shape reconstruction problem [1, 2]. On the other hand, for penetrable objects such as dielectric materials in electromagnetics, one has to establish a solution approach in order to recover shape and/or electrical constitutive parameters [1, 2]. Although these two major groups in inverse scattering problems have been extensively studied in the open literature, fast and effective solution approaches are still required. In this thesis, we will present two novel shape reconstruction methods for perfect electric conducting targets which is in the first group.

Beside their significance in many engineering areas, these inverse problems have a remarkable theoretical aspect that they are mostly *ill-posed* [2] and nonlinear thus solution approaches have to handle these properties in an appropriate way. In the sense of Hadamard's postulates, well-posedness of a problem is defined by the following conditions:

1. Existence of the solution

1

2. Uniqueness of the solution

3. Continuous dependence of the solution on the input data

If a problem inherently does not have one of these crucial properties, it is classified as *ill-posed* or *improperly-posed*. Mathematically, it is possible to enforce the existence of a solution by enlarging the solution space and the uniqueness can be cured by introducing additional constraints on the solution [1]. Among these criteria, continuous dependence to the input data is most restrictive. As the solution exhibits strong sensitivity to small perturbations on the input data, it becomes practically impossible to calculate a solution when the input data is provided through measurements of a physical process where the noise is inevitable. Therefore the solution of an ill-posed problem requires imposing certain constraints on the problem, and in most cases only an approximate solution can be achieved. The procedure of getting an approximate but stable solution for an ill-posed problem is called *regularization*. Well known methods include Tikhonov regularization and truncated singular value decomposition (TSVD). These regularization methods are function of a regularization parameter whose selection provides a trade-off between accuracy and stability of the solution. Optimal selection of the regularization parameter generally requires a priori knowledge on the expected noise level of the measured data. If there is no a priori information available, then only choice for selecting the regularization parameter becomes trial and error such that the inverse problem is solved for a set of regularization parameters and the most reasonable solution is selected [2].

1.1 Reconstructing the Shape of Inaccessible Objects

As mentioned, retrieving the shape and the location of inaccessible objects from a set of far field measurements constitutes one of the basic problems in inverse scattering theory. Accordingly, such problems have been extensively investigated in the open literature. Since the very first attempts for the solution [3, 4], many methods based on different approaches such as physical optics theory [5–7], Newton-Kantorovich method [8], equivalent source method [9], analytical continuation methods (decomposition methods) [10–15], linear sampling method [16–21], factorization method [22, 23], probe method [24], singular source method [25, 26], no response test [27], range-test method [28], level set method [29], metaheuristic

optimization based methods [30, 31] have been developed. Most of these methods can be roughly classified into three major groups:

a) Iterative Methods:

These methods require a priori knowledge of the boundary conditions which is employed on the surface of inaccessible objects. By using the boundary conditions, the shape reconstruction method is formulated as a minimization of a nonlinear ill-posed operator equation, then iterative schemes such as regularized Newton methods, Landweber iterations or conjugate gradient methods are applied for its solution. These methods work with minimum amount of singleview data at a fixed frequency and provide reasonable reconstructions when the noise level of measured data is sufficiently low. However these methods generally requires to solve forward problem at least once at each iteration step which makes them impractical in most cases. As a minimization problem, these methods also suffer from local minimums depending on selection of initial guesses. Examples of iterative methods include Newton-Kantorovich method [8], metaheuristic optimization based methods [30, 31].

b) Sampling and Probe Methods:

The sampling methods do not model directly the physical scattering phenomena. On the other hand this conceptional difference provides their major advantage over other methods. In theory, sampling methods does not require any a-priori knowledge about boundary conditions. The sampling methods based on the numerical evaluation of an indicator function over a domain where the objects are searched. Major disadvantage of sampling methods is that they need large amount of multiview data and do not provide sharp reconstructions as compared to other methods. Well known sampling methods include the linear sampling method [16–20], the factorization method [22, 32] which is related to linear sampling method, probe method [24], singular source method [25, 26], no response test [27] and range-test method [28].

c) Decomposition or Analytical Continuation Methods:

The decomposition or analytical continuation methods handles the ill-posedness and the nonlinearity of the underlying inverse scattering problem separately [10–15]. Initially, an ill-posed linear operator is used to reconstruct the scattered field in the vicinity of the obstacle from its measured far field. To this aim regularized single-, double- or mixed layer potential approaches are generally employed. Then by using the

3

boundary conditions, the shape reconstruction problem is formulated as a minimization of nonlinear equation of the shape. These methods share similar characteristics with iterative methods however their major advantage over iterative methods that they do not require to solve forward problem at each iteration. Thus they can be considered as improved versions of iterative methods.

1.2 The Aim of the Study

Although the shape reconstruction methods mentioned in section 1.1 had made important contributions to solution of inverse obstacle scattering problem, the problem of accurately retrieving geometrical properties of the unknown objects with a limited amount of far field data is still a very active research area due to importance of possible applications.

Within this framework, the objective of this thesis is to develop new and efficient methods to reconstruct the shape of inaccessible, electrically conducting structures by utilizing the scattered field measurements performed in the far-field region. Consequently, two new shape reconstruction schemes which are in the class of analytical continuation methods are developed for imaging perfect electric conducting targets.

The first method is based on the analytical continuation of the scattered field by means of single layer potential representation and Taylor series expansion. In particular, the measured far-field data which is corrupted with inevitable measurement noise, first backpropagated to a circular domain enclosing the inaccessible object in terms of regularized inversion of a single layer potential. The reconstructed single layer potential density enables to approximate scattered field outside of the encircled object quite accurately, while a Taylor series expansion in the radial direction is exploited to represent the field in the vicinity of the target. From the boundary condition that the total electric field vanishes on the surface of the target, the problem is then recast as a polynomial equation containing the contour of the object as an unknown. Later this nonlinear equation is iteratively solved via the Gauss-Newton algorithm to retrieve the unknown shape.

The second method introduced in this thesis is based on creating an equivalent scattering problem in terms of standard impedance boundary condition (SIBC). More

precisely, the unknown perfectly conducting target is equivalently modeled as a circular impedance cylinder, having inhomogeneous surface impedance. By virtue of equivalence, the impedance cylinder generates the same field distribution on whole space outside of the unknown object, as long as the latter is enclosed by the unknown target to be reconstructed. In order to determine the equivalent surface impedance, first the noise corrupted measured far-field data is backpropagated to the surface of the equivalent impedance cylinder, through the regularized inversion of the single-layer potential. Then, the surface impedance is recovered by exploiting the SIBC imposed over the impedance cylinder which requires the total electric and magnetic field values on the boundary. Since the reconstructed surface impedance enables to represent scattered field outside of the unknown target, the retrieval of the unknown shape turns out to be the solution of a nonlinear optimization problem, which is solved iteratively through the Gauss-Newton algorithm.

The organization of thesis is as follows: In chapter 2 details of the shape reconstruction problem and preliminary definitions required to formulate the solutions are described. Then, the shape reconstruction algorithm for conducting objects which is based on the analytical continuation of scattered field in terms of Taylor series expansions is introduced in chapter 3. The concept of the modeling unknown scatterer by means of inhomogeneous surface impedance, and the usage of this equivalent impedance in shape reconstruction is addressed in chapter 4. In chapter 5 several numerical results are demonstrated to show the validity and the capabilities of the both shape reconstruction methods. The results achieved are concluded in chapter 6. Through the thesis, time factor $e^{-i\omega t}$ is assumed and factored out.

2. SHAPE RECONSTRUCTION PROBLEM FOR INACCESSIBLE, PERFECT ELECTRIC CONDUCTING TARGETS

In this chapter, the details of the inverse scattering problem which is investigated through this thesis and the associated assumptions which are necessary to formulate the shape reconstruction methods, later presented in chapter 3 and chapter 4, are explained.

2.1 Inverse Obstacle Scattering Problem for 2D Case

Through the thesis, only two dimensional scattering problem illustrated in figure 2.1 is considered, hence it is assumed that the shape of the scatterer does not change at Ox_3 direction and the scatterer is infinitely long at that direction in terms of the operating wavelength λ. In this configuration, D is a perfectly conducting cylindrical body whose boundary ∂D is assumed to be starlike shape, i.e., an arbitrary point on ∂D can be represented in polar coordinates as $(f(\phi), \phi)$ where $f(\phi)$ is a real single-valued function of $\phi \in [0, 2\pi)$. The body D is located in a homogeneous infinite space whose electromagnetic constitutive parameters are ε, μ and σ.

The inverse scattering problem considered here consists in recovering the boundary of the object ∂D, i.e., the function $f(\phi)$, from a set of far field measurements of the scattered wave. To this aim, the body D is illuminated with a time-harmonic plane wave whose electric field vector $\mathbf{E}^i$ is always parallel to the Ox_3 axis. This field is given by:

$$\mathbf{E}^i = \left(0, 0, u^i(\mathbf{x})\right) \tag{2.1}$$

with

$$u^i(\mathbf{x}) = e^{-ik\mathbf{x}.\mathbf{d}}, \quad \mathbf{x} \in \mathbb{R}^2 \tag{2.2}$$

where $\mathbf{d} = (\cos\theta, \sin\theta)$ is the propagation direction with incidence angle θ and wavenumber k which is the square root of $k^2 = \omega^2\varepsilon\mu + i\omega\sigma\mu$. Due to the homogeneity in the Ox_3 direction, the total and scattered electric field vectors will have only x_3 components, thus the problem is reduced to a scalar case.
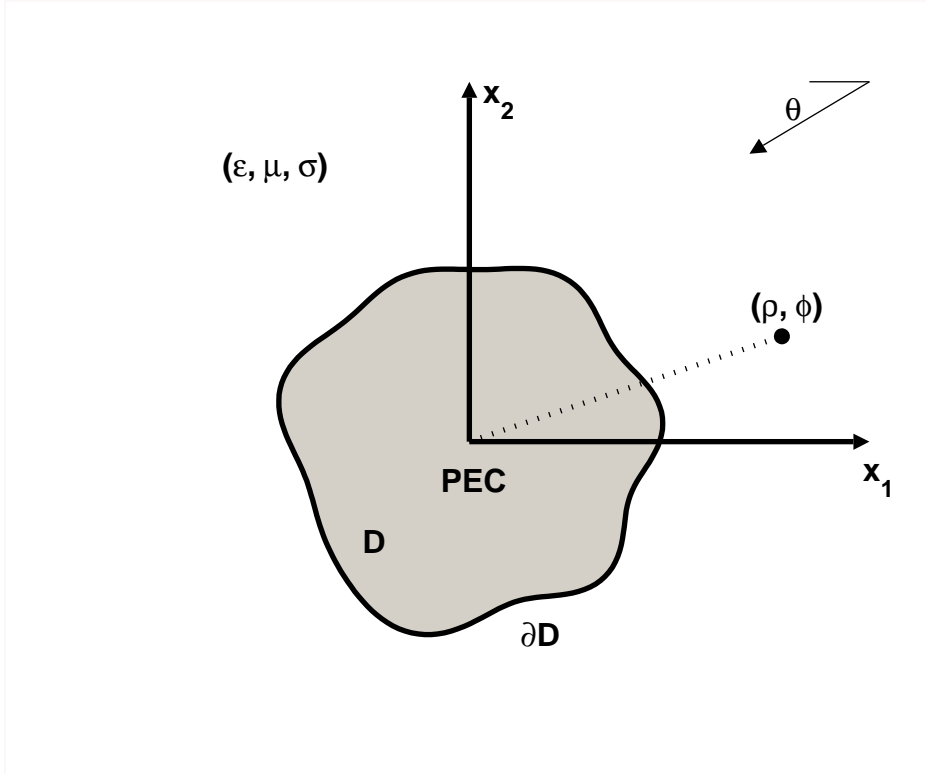
Figure 2.1: 2D cross section of the problem geometry which is considered for shape reconstruction of PEC objects.

Let $u(\mathbf{x})$ denote the total electric field then the scattered field, $u^s(\mathbf{x})$, is defined as the difference between total field and the incident field

$$u^s(\mathbf{x}) = u(\mathbf{x}) - u^i(\mathbf{x}) \tag{2.3}$$

and satisfies the Helmholtz equation

$$\Delta u^s(\mathbf{x}) + k^2 u^s(\mathbf{x}) = 0, \quad \mathbf{x} \in \mathbb{R}^2 \setminus \overline{D} \tag{2.4}$$

with the boundary condition

$$u(\mathbf{x}) = 0, \quad \mathbf{x} \in \partial D. \tag{2.5}$$

In addition $u^s(\mathbf{x})$ satisfies the Sommerfeld radiation condition

$$\lim_{r \to \infty} \sqrt{r} \left(\frac{\partial u^s}{\partial r} - iku^s \right) = 0, \quad r = |\mathbf{x}| \tag{2.6}$$

and has an asymptotic behavior of the form

$$\lim_{|\mathbf{x}| \to \infty} u^s(\mathbf{x}) = \frac{e^{ik|\mathbf{x}|}}{\sqrt{|\mathbf{x}|}} \left\{ u^\infty(\hat{x}) + \mathcal{O}\left(\frac{1}{|\mathbf{x}|} \right) \right\}, \quad \hat{\mathbf{x}} = \frac{\mathbf{x}}{|\mathbf{x}|} \tag{2.7}$$

uniformly in all directions. The function $u^\infty(\hat{\mathbf{x}})$ is known as far field pattern of the scattered field.

Here the direct scattering problem is defined as the determination of the scattered field $u^s(\mathbf{x})$ or its asymptotic form $u^\infty(\hat{\mathbf{x}})$ provided that the boundary ∂D and the incident field $u^i(\mathbf{x})$ is known. This problem is well-posed and the uniqueness of the solution can be proven under the assumption that $Im(k) > 0$ [33]. To solve the direct problem related to arbitrary shaped obstacles, several numerical methods such as boundary integral equations, finite element method are applicable.

The corresponding inverse scattering problem is defined as the retrieval of the boundary ∂D from a given set of far field $u^\infty(\hat{\mathbf{x}})$ data. This is a well-known ill-posed problem and as pointed out in the introduction, several methods based on quite different approaches have already been established. However due to the nature of the inverse problem, there is no general solver which can handle all kind of configurations. The uniqueness of the solution is proven under quite restrictive assumptions on the size of the obstacle and on the variation of its boundary [2].

2.2 Surface Potentials

Through the thesis, surface potentials [33] have been extensively used. Thus basic definitions are summarized here.

The Green's function $G(\mathbf{x}, \mathbf{y})$ for the Helmholtz equation is the solutions of

$$\Delta G(\mathbf{x}, \mathbf{y}) + k^2 G(\mathbf{x}, \mathbf{y}) = -\delta(\mathbf{x} - \mathbf{y}), \quad \mathbf{x} \neq \mathbf{y}, \tag{2.8}$$

and is given by

$$G(\mathbf{x}, \mathbf{y}) = \frac{i}{4} H_0^{(1)}(k|\mathbf{x} - \mathbf{y}|), \quad \mathbf{x} \in \mathbb{R}^2 \setminus \{\mathbf{y}\} \tag{2.9}$$

where $H_0^{(1)}(.)$ denotes the zero order Hankel function of the first kind. It has an asymptotic form as $|\mathbf{x} - \mathbf{y}| \to \infty$

$$\lim_{|\mathbf{x}-\mathbf{y}|\to\infty} G(\mathbf{x}, \mathbf{y}) = \frac{e^{i\pi/4}}{\sqrt{8\pi k|\mathbf{x} - \mathbf{y}|}} e^{ik|\mathbf{x}-\mathbf{y}|} \left\{ 1 + \mathscr{O}\left(\frac{1}{|\mathbf{x} - \mathbf{y}|}\right) \right\} \tag{2.10}$$

and has a logarithmic singularity when source and observer points coincide

$$\lim_{|\mathbf{x}-\mathbf{y}|\to 0} G(\mathbf{x}, \mathbf{y}) = \frac{1}{2\pi} \ln\left(\frac{1}{|\mathbf{x} - \mathbf{y}|}\right) + \frac{i}{4} - \frac{1}{2\pi} \ln\left(\frac{k}{2}\right) - \frac{C}{2\pi} + \mathscr{O}\left(|\mathbf{x} - \mathbf{y}|^2 \ln\frac{1}{|\mathbf{x} - \mathbf{y}|}\right)$$
$$\tag{2.11}$$

where $C = 0.577215...$ is an irrational number known as Euler-Mascheroni constant. In the numerical evaluation of the Green's function, a special treatment is required to avoid this singularity.

The single-layer potential and the double-layer potential are defined as

$$u(\mathbf{x}) := \int_{\partial D} G(\mathbf{x}, \mathbf{y}) \psi(\mathbf{y}) \mathrm{d}s(\mathbf{y}), \quad \mathbf{x} \in \mathbb{R}^2 \setminus \partial D \tag{2.12}$$

and

$$v(\mathbf{x}) := \int_{\partial D} \frac{\partial G(\mathbf{x}, \mathbf{y})}{\partial n(\mathbf{y})} \varphi(\mathbf{y}) \mathrm{d}s(\mathbf{y}), \quad \mathbf{x} \in \mathbb{R}^2 \setminus \partial D \tag{2.13}$$

respectively, where $\psi(\mathbf{x})$ and $\varphi(\mathbf{y})$ are called single- and double-layer potential densities respectively and $n(\mathbf{y})$ denotes outward surface normal. It is proved that any solution to Helmholtz equation can be represented as a combination of single- and double-layer potentials [33] and these potentials satisfy the Sommerfeld radiation condition (2.6) as well. The single- and double-layer potentials can be extended to the boundary by means of jump relations [33] and one has

$$u_{\pm}(\mathbf{x}) = \int_{\partial D} G(\mathbf{x}, \mathbf{y}) \psi(\mathbf{y}) \mathrm{d}s(\mathbf{y}), \quad \mathbf{x} \in \partial D \tag{2.14}$$

$$\frac{\partial u_{\pm}}{\partial n}(\mathbf{x}) = \int_{\partial D} \frac{\partial G(\mathbf{x}, \mathbf{y})}{\partial n(\mathbf{x})} \psi(\mathbf{y}) \mathrm{d}s(\mathbf{y}) \mp \frac{1}{2} \psi(\mathbf{x}), \quad \mathbf{x} \in \partial D \tag{2.15}$$

$$v_{\pm}(\mathbf{x}) = \int_{\partial D} \frac{\partial G(\mathbf{x}, \mathbf{y})}{\partial n(\mathbf{y})} \varphi(\mathbf{y}) \mathrm{d}s(\mathbf{y}) \pm \frac{1}{2} \varphi(\mathbf{x}), \quad \mathbf{x} \in \partial D \tag{2.16}$$

where subscripts $+$ and $-$ denotes to the limits obtained by approaching the boundary ∂D from outside of D and inside of D, respectively.

3. SHAPE RECONSTRUCTION BY ANALYTICAL CONTINUATION OF THE SCATTERED FIELD THROUGH TAYLOR SERIES EXPANSION

In this section, a new shape reconstruction method for inaccessible PEC targets is presented. The method basically consists of two steps. The first step aims to obtain an approximate scattered field variation in the vicinity of the target to be reconstructed from the given, noise corrupted far field pattern of the scattered wave, while the second step is to reduce the problem into solution of a nonlinear system of equations through the use of boundary condition on the surface of the unknown object.

In the first step, by utilizing the single-layer potential representation (2.12), the far field pattern is modeled as if it is generated by an unknown potential density on the boundary of a circular cylinder which is assumed to cover the unknown target with a preferably minimum radius. The resulting Fredholm integral equation of first kind is ill-posed. Thus it is inverted in a regularized fashion via truncated singular value decomposition in order to solve the unknown single-layer potential density. With the reconstructed potential density, it possible to calculate the approximate scattered field in whole space outside of the minimum circle, while a Taylor series expansion of the scattered field is exploited inside the minimum circle in the radial direction to get the scattered field in the vicinity of the target.

At the final step, the Taylor series expansion together with the boundary condition that the total field on boundary of the unknown target must vanish, is used to get a polynomial equation which contains the shape of the target as unknown. This nonlinear equation is solved iteratively with Gauss-Newton algorithm with the initial guess chosen as the minimum circle. As demonstrated in chapter 5, the presented method provides accurate reconstructions for both convex and concave obstacles even when signal-to-noise ratio (SNR) is low. With a careful implementation, the method is quite fast since the nonlinear equation is in a polynomial form and the coefficients containing the derivatives of the scattered field become constants in the iteration

procedure. Moreover only a few terms in the Taylor series expansion are enough when the variation of the boundary is small in terms of the operating wavelength.

3.1 Backpropagation of the Scattered Field by Single-Layer Potential Representation

As mentioned earlier, it is first considered a circle with radius $\rho = \alpha$ which separates the space outside of the object into two parts i.e $\rho > \alpha$ and $f(\phi) < \rho < \alpha$. In the exterior domain $\rho > \alpha$, the scattered wave is expressed as a single-layer potential of the form

$$u^s(\rho,\phi) = \frac{i}{4} \int_0^{2\pi} H_0^{(1)} \left(k\sqrt{\rho^2 + \alpha^2 - 2\rho\alpha\cos(\phi-\tau)} \right) \Psi(\tau)\alpha d\tau, \quad \rho > \alpha \qquad \textbf{(3.1)}$$

with an unknown potential density function $\Psi(\tau)$ on the circle $\rho = \alpha$. For the sake of simplicity, it is assumed that k^2 is not at interior resonance, that is, k^2 is not a Dirichlet eigenvalue for the negative Laplacian in D. In this case, any solution to the Helmholtz equation in the exterior of D that satisfies the radiation condition (2.6) can be indeed represented as a single-layer potential [2]. Note that, in order to avoid the mentioned restriction, one would need to replace the single-layer potential by a combined single- and double-layer potentials [2]. In the inverse scattering problem considered here, the scattered field is known in the far field region and (3.1) can be written in compact form as follows:

$$S\Psi = u^\infty \qquad \textbf{(3.2)}$$

for the unknown density Ψ. By using the asymptotic form of Hankel function of the first kind [34], the integral operator S is represented by

$$(S\Psi)(\phi) = \frac{e^{i\pi/4}}{\sqrt{8\pi k}} \int_0^{2\pi} e^{-ik\cos(\phi-\tau)}\Psi(\tau)\alpha d\tau. \qquad \textbf{(3.3)}$$

Since S is a linear compact operator, (3.2) is severely ill-posed [2]. For this reason, a kind of regularization has to be applied and only an approximation of the sought function Ψ can be achieved [2, 35].

A convenient tool to solve (3.2) is provided by the Singular Value Decomposition (SVD) [35]. For a linear compact operator S, the SVD is defined as the triple
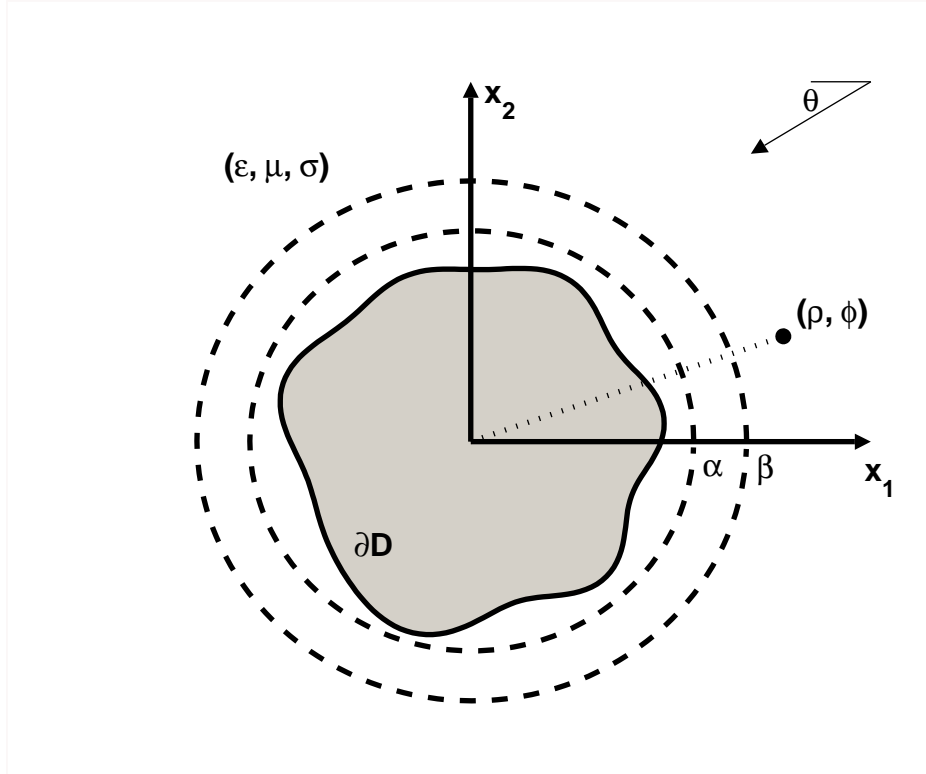
Figure 3.1: The problem geometry for the shape reconstruction method based on Taylor series expansion. α: radius of the minimum circle, β: radius of the circle where the scattered field is expanded to Taylor series.

$\{\sigma_r, \varphi_r, v_r\}$ such that:

$$S\Psi = \sum_{r=1}^{\infty} \sigma_r \langle \Psi, \varphi_r \rangle v_r \tag{3.4}$$

which provides the explicit inversion formula

$$\Psi = \sum_{r=1}^{\infty} \frac{1}{\sigma_r} \langle u^{\infty}, v_r \rangle \varphi_r \tag{3.5}$$

where $\langle, \rangle$ denotes the inner product in the proper space. Due to the properties of the kernel of the operator S, the singular values σ_r accumulate to zero exponentially fast as $r \to \infty$ [35, 36]. In presence of uncertainties on data, this behavior leads to unstable solutions, as contributions related to high order singular values are completely overwhelmed by noise [35]. A possible way to overcome this instability is given by the regularized solution provided by truncated SVD (TSVD) inversion formula:

$$\Psi^{(R)} = \sum_{\sigma_r \geq \sigma_R} \frac{1}{\sigma_r} \langle u^{\infty}, v_r \rangle \varphi_r \tag{3.6}$$

in which the truncation index R acts as regularization parameter. In particular, accuracy of the approximation introduced in (3.6) requires R to be large enough, whereas in

order to restore stability and reduce the effects of noise R is needed to be small enough. Consequently, selecting a proper regularization parameter is crucial on the accuracy of the reconstructed scattered field. In order to tackle this tradeoff, one can exploit the Morozov's discrepancy principle [37]

$$||S\Psi^{(R)} - \tilde{u}^{\infty}||^2 \leq \delta, \tag{3.7}$$

which provides a practical strategy to select a proper regularization parameter when a priori knowledge is available for expected noise power δ.

By applying TSVD inversion (3.6) to (3.3), one can reconstruct the single-layer density $\Psi(\mathbf{y})$ which yields to obtain the scattered field and consequently the total field $u(\rho, \phi)$ in the region $\rho > \alpha$ from the measured values of the far field pattern $u^{\infty}(\phi)$. However, due to the above mentioned "smoothing" properties of the kernel of the operator S, this reconstructed field would actually be a low-pass version of the actual one. In particular, as the field in the vicinity to the boundary ∂D is expected to have a larger high-frequency spectral content [38], the accuracy of this approximation worsens as $\rho \to \alpha$. As it will be shown in the following, this circumstance has also to be taken into account in the choice of R. Interestingly, as this undesired and unavoidable loss of accuracy in the reconstruction of the close-proximity scattered field is less critical for scatterers whose size is comparable or lower than the working wavelength [38], in the following only this class of scatterers is considered. Numerical implementation of TSVD inversion is later discussed in Appendix A.

3.2 Analytical Continuation of the Scattered Field through Taylor Series Expansion

Let us now turn to the interior region $f(\phi) < \rho < \alpha$. Within the approximation introduced by the TSVD inversion and the above recalled limitations concerning the size of the body, the total field in this region can be obtained by using the field $u^s(\rho, \phi)$ given by (3.1). In particular, $u(\rho, \phi)$ is expanded into a Taylor series in terms of ρ around the circle $\rho = \beta$, where $\alpha \leq \beta$, see figure 3.1, as follows [39, 40]:

$$u(\rho, \phi) = e^{-ik\rho\cos(\phi - \theta)} + \sum_{m=0}^{M} c_m (\rho - \beta)^m + R_M(\rho, \phi), \quad \rho \in (f(\phi), \beta] \tag{3.8}$$

with coefficients

$$c_m = \frac{1}{m!} \frac{\partial^m u^s(\beta, \phi)}{\partial \rho^m} \tag{3.9}$$

14

and remainder term

$$R_M(\rho,\phi) = \frac{1}{M!} \int_\beta^\rho (\rho-\rho')^M \frac{\partial^{M+1} u^s(\rho',\phi)}{\partial\rho'^{M+1}} d\rho'. \tag{3.10}$$

The m'th order derivatives of $u^s(\rho,\phi)$ at $\rho = \beta$ appearing in the right hand side of (3.9) can be obtained from (3.1) and one has

$$\frac{\partial^m u^s(\beta,\phi)}{\partial\rho^m} = \frac{i\alpha}{4} \int_0^{2\pi} \frac{\partial^m}{\partial\rho^m} \left[H_0^{(1)}(k\sqrt{\rho^2+\alpha^2-2\rho\alpha\cos(\phi-\tau)}) \right]\Big|_{\rho=\beta} \Psi(\tau)d\tau \tag{3.11}$$

Although $u(\rho,\phi)$ is a regular function of ρ, in general, the remainder term in (3.8) does not necessarily tend to zero for all $\rho \in (f(\phi),\beta]$, that is, the corresponding Taylor series does not always converge down to the surface ∂D. Nevertheless, by neglecting the remainder, the Taylor formula is exploited as an approximation within the inverse algorithm described later.

It should be noted that $u(\rho,\phi)$ could also be expanded into a Taylor series around the minimum circle $\rho = \alpha$. However, in such a case, the integral appearing in the right hand side of (3.11) becomes singular due to logarithmic singularity of the Hankel function (2.11) as its argument goes to zero. Thus it becomes quite difficult to evaluate, especially for higher order derivatives of $u(\alpha,\phi)$. Hence, to avoid this difficulty, the scattered field is expanded to the Taylor series around the circle $\rho = \beta > \alpha$.

3.3 Reconstruction Algorithm for Singleview Case

Since the total field $u(\rho,\phi)$ in the whole region $\rho > f(\phi)$ can be estimated through (3.1) and (3.8), the reconstruction of the boundary ∂D can now be achieved by searching those points where the total field vanishes. Substituting (3.8) in (2.5) and neglecting the remainder term (3.10) yields

$$F_M(f) = 0 \tag{3.12}$$

where F_M is the nonlinear operator given by

$$F_M(f) = e^{-ikf\cos(\phi-\theta)} + \sum_{m=0}^{M} c_m (f-\beta)^m. \tag{3.13}$$

Note that, for given data, the coefficients c_m in (3.13) are all known through the relation (3.11). Thus the reconstruction problem is reduced to the solution of nonlinear equation (3.12) for the unknown function f.

15

The accuracy of the Taylor series in (3.8) (neglecting the remainder for $\rho = f(\phi)$) is related to $\frac{|\rho - \beta|}{\lambda}$, which is the distance between the surface ∂D and the circle $\rho = \beta$ for a certain ϕ. If the circle $\rho = \beta$ is close to the surface (with respect to the wavelength) and the surface function $f(\phi)$ is a slightly varying one, the distance $|f(\phi) - \beta|$ becomes small. Therefore, provided that the above condition (which entails some limitations on the angular variability of the unknown profiles) is fulfilled, the number M which is the truncation number of the series (3.8) can be small. To select the appropriate M, a threshold value δ is chosen and the series (3.8) is truncated at the smallest M satisfying

$$\left| c_M \left(\min[f(\phi)] - \beta \right)^M \right| < \delta. \tag{3.14}$$

As this expression requires a knowledge of $f(\phi)$, which is the unknown of the problem, from a practical point of view an estimate of M can be achieved by substituting $\min[f(\phi)] = \alpha/2$ into (3.14).

The nonlinear equation (4.32) is solved iteratively via Newton method [40]. Hence, for an initial guess f_0, the nonlinear equation (3.12) is replaced by the linearized equation

$$F_M(f_0) + F'_M(f_0)\Delta f = 0 \tag{3.15}$$

where $\Delta f = f - f_0$, which needs to be solved for Δf in order to improve an approximate boundary ∂D given by the function f_0 into a new approximation with surface function $f_0 + \Delta f$. In (3.15) F'_M denotes the Fréchet derivative of the operator F_M with respect to f [2]. It can be shown that F'_M reduces to the ordinary derivative of F_M with respect to f.

The Newton method consists in iterating this procedure, i.e.: solving

$$F'_M(f_i)\Delta f_{i+1} = -F_M(f_i), \quad i = 0, 1, 2, \ldots \tag{3.16}$$

for Δf_{i+1} to obtain a sequence of approximations through $f_{i+1} = f_i + \Delta f_{i+1}$. As this solution will be sensitive to errors in the derivative of F_M in the vicinity of zeros, a finite dimensional approximation of Δf is looked for in order to obtain a stable procedure. In particular, the approximated solution is expressed in terms of a linear combination of some basis functions $\vartheta_p(\phi)$, $p = 1, \ldots, P$, as

$$\Delta f(\phi) = \sum_{p=1}^{P} a_p \vartheta_p(\phi). \tag{3.17}$$

Then (3.15) is satisfied in the least squares sense, that is, the coefficients $a_1, \ldots, a_P$ in (3.17) are determined so that for a set of grid points $\phi^1, \ldots, \phi^J$ the sum of squares

$$\sum_{j=1}^{J} \left| F'_M(f(\phi^j)) \sum_{p=1}^{P} a_p \vartheta_p(\phi^j) + F_M(f(\phi^j)) \right|^2 \tag{3.18}$$

is minimized.

The number of basis functions P in (3.17) can be considered as a further regularization parameter. As a matter of fact, choosing P too large may lead to instabilities due to the ill-posedness of the underlying inverse problem, while choosing P too small would result in poor approximation quality. On the other hand, a reduction of the number P of unknown coefficients has a beneficial effect in reducing occurrence of false solutions, which may arise due to the nonlinearity of the problem. Hence, one has to compromise between stability and accuracy and in this sense P serves as a regularization parameter.

3.4 Reconstruction Algorithm for Multiview Case

The reconstruction algorithm explained in section 3.3 is designed to exploit singleview data corresponding to a single illumination at a fixed frequency but it cannot utilize multiview data when more than one illumination is employed. In such a case, one may attempt to solve the inverse scattering problem for each illumination, then averaging the reconstructions to achieve a final solution. Although it may provide a reasonable reconstruction depending on the noise level, the improvement of the reconstruction quality is limited [41]. Instead here a global solution which can utilize all the available data simultaneously is searched for. This is quite important since the unknown boundary ∂D is actually independent from the source excitation. Moreover as it will be demonstrated later in chapter 5, by exploiting multiview data, it becomes possible to reconstruct larger targets in terms of wavelength, which are not possible with singleview data.

Let $u_n(x)$ denote the total field corresponding to n'th illumination with incidence angle θ_n. For each illumination, the procedure explained in section 3.3 provides a complete characterization of the field in whole region exterior to the target. Therefore, since the total field $u_n(\rho, \phi)$ for any $\rho > f(\phi)$ can be estimated through (3.1) and (3.8), the reconstruction of the boundary ∂D can be achieved by searching those points where, according to the boundary condition, this latter field vanishes.

As given in the previous section, for a single illumination θ_n, the above can be formulated as the solution of the nonlinear equation which arises from the Taylor series expansion (3.8) by neglecting the remainder term:

$$F_n(f) = e^{-ikf\cos(\phi-\theta_n)} + \sum_{m=0}^{M} c_m^{(n)}(f-\beta)^m. \tag{3.19}$$

where the truncation index M can be small provided the unknown shape is sufficiently smooth [13]. As the operator in (3.19) changes with the incidence direction, for each illumination, a different solution for the surface function f, say f_n, is solved. On the other hand, the function f is actually independent of the illumination direction, so that one can simultaneously exploit all the multiview data by simply recasting the problem as the system of nonlinear equations:

$$
\begin{aligned}
&F_1(f) = 0 \\
&\qquad . \\
&\qquad . \\
&\qquad . \\
&F_N(f) = 0
\end{aligned}
\tag{3.20}
$$

for the unknown surface function f.

The nonlinear system (3.19) is solved iteratively via Gauss-Newton algorithm [42]. In particular, given an initial guess f_0, at each iteration one has to solve the system arising from linearization of (3.19) in the Newton sense [13]:

$$
\begin{pmatrix} F_1'(f_i) \\ . \\ . \\ . \\ F_N'(f_i) \end{pmatrix} \Delta f_{i+1} = - \begin{pmatrix} F_1(f_i) \\ . \\ . \\ . \\ F_N(f_i) \end{pmatrix}
\tag{3.21}
$$

where f_i is the estimated shape at the i-th iteration and Δf_{i+1} provides the updated shape $f_{i+1} = f_i + \Delta f_{i+1}$. In (3.21) the term F_n' denotes the Fréchet derivative of F_n with respect to f_i, which reduces to the ordinary derivatives since in the present cases the operators are the polynomials of f_i.

In a similar manner to the reconstruction algorithm in singleview case, the solution of the linear system (3.21) is sensitive to errors in the derivative of F_N' in the vicinity of zeros. Thus a finite dimensional solution is sought by expanding Δf to a series as in (3.17). Then, by substituting (3.17) into (3.21) and discretizing ϕ into Q collocation points $\phi_1, \ldots \phi_Q$, the system is recast 3.21 in a matrix form as:

$$\mathbf{J}_F(f_i)\mathbf{x}_{i+1} = -\mathbf{V}(f_i), \tag{3.22}$$

which leads to the least squares solution

$$\mathbf{x}_{i+1} = -\left[\mathbf{J}_F^*(f_i)\mathbf{J}_F(f_i)\right]^{-1}\mathbf{J}_F^*(f_i)\mathbf{V}(f_i). \tag{3.23}$$

In (3.22) and (3.23), the column vector $\mathbf{x}_{i+1}$ contains the P coefficients of the expansion (3.17), the $(N \times Q) \times P$ matrix $\mathbf{J}_F$ denotes the projection of the matrix F' over the basis functions, the $(N \times Q) \times 1$ column vector $\mathbf{V}$ corresponds to the value of F at collocation points and $\mathbf{J}_F^*$ is the adjoint of the matrix $\mathbf{J}_F$. For a fixed threshold δ, the iterative process is stopped when the condition $||x_{i+1} - x_i|| < \delta$ is satisfied.

4. SHAPE RECONSTRUCTION BY INHOMOGENEOUS SURFACE IMPEDANCE MODELING

The impedance boundary conditions (IBC) provide a relation between the electric and the magnetic field vectors on a given structure in terms of surface impedances [43, 44]. In general, the surface impedance is a tensor which can be reduced to an inhomogeneous scalar under certain assumptions. In scattering theory, IBCs are essential tools to model electromagnetic characteristics of complex materials in order to simplify the formulations and reduce computational costs [45, 46]. To determine the surface impedance for a given scatterer, the general approach consist of first solving direct electromagnetic scattering problem and then obtaining the surface impedance from the electric and the magnetic field vectors on a given surface. To this aim, various analytical and approximate methods for canonical geometries have been established in the open literature [43, 44]. On the other hand, the surface impedance of a scatterer can also be obtained by using the scattered field collected through measurements on a certain domain. In such a case, it is considered as an inverse scattering problem whose aim is to get the electric and the magnetic fields on the boundary of the object in terms of the measured data [47–49].

Within this framework, here the aim is to develop a new shape reconstruction method based on creating an equivalent scattering problem in terms of standard impedance boundary condition (SIBC). In particular, the unknown perfect conducting target is modeled as a circular impedance cylinder, having inhomogeneous surface impedance. As a matter of fact, as long as the impedance cylinder is enclosed inside the unknown target, by virtue of equivalence, the two scatterers generate same field distribution in the whole space outside of the unknown target. In order to determine the equivalent surface impedance, first the measured far-field data which are corrupted with noise, are backpropagated to the surface of the equivalent impedance cylinder through the regularized inversion of the single-layer potential [48]. Then, the surface impedance is recovered by exploiting the SIBC imposed over the impedance cylinder. Since the

reconstructed surface impedance enables to represent scattered field outside of the unknown target, the retrieval of the unknown shape turns out to be the solution of a nonlinear optimization problem, which is solved iteratively via the Gauss-Newton algorithm [14].

4.1 Equivalent Representation of the Unknown Target in Terms of Inhomogeneous Surface Impedance

This section is devoted to discussion of creating an equivalent direct scattering problem in terms of inhomogeneous surface impedance modeling. As illustrated in figure 4.1 the problem configuration is same with the previous configuration explained in section 2.1.

Let $u_n^\infty(\hat{\mathbf{x}})$ denote the far field pattern of the scattering wave from the PEC target D, corresponding to n'th illumination ($n = 1, 2, ..., N$) with an incidence angle θ_n. Here the main focus is to determine the normalized surface impedance $\eta_n(\mathbf{x})$ from $u_n^\infty(\hat{\mathbf{x}})$ on an impedance cylinder with radius $|\mathbf{x}| = \gamma$ which generates the same field distribution in the region outside of ∂D. To this aim, the impedance reconstruction algorithm [48], which is briefly summarized below, is exploited.

It is assumed that on the surface of the equivalent object the standard impedance boundary condition [50],

$$-\hat{\mathbf{n}} \times (\hat{\mathbf{n}} \times \mathbf{E}) = Z(\mathbf{x})\, \hat{\mathbf{n}} \times \mathbf{H}, \tag{4.1}$$

is satisfied, where $\mathbf{E}$ and $\mathbf{H}$ are the total electric and magnetic field vectors and $\hat{\mathbf{n}}$ is the outward unit normal vector. In (4.1) $Z(\mathbf{x})$ is the surface impedance to be determined which is assumed to be a function of the location. It can be proven that (refer to appendix B) in the problem configuration (4.1) is reduced to a scalar relationship

$$\frac{\partial u}{\partial n}(\mathbf{x}) + \frac{ik}{\eta(\mathbf{x})} u(\mathbf{x}) = 0, \tag{4.2}$$

where $\eta(\mathbf{x})$ is the normalized surface impedance defined by

$$\eta(\mathbf{x}) = \frac{Z(\mathbf{x})}{Z_0}, \tag{4.3}$$

and $Z_0 = \sqrt{\frac{\mu}{\varepsilon'}}$ denotes the intrinsic impedance of the background medium with ε' being the complex dielectric permittivity. Since both problems have the same field
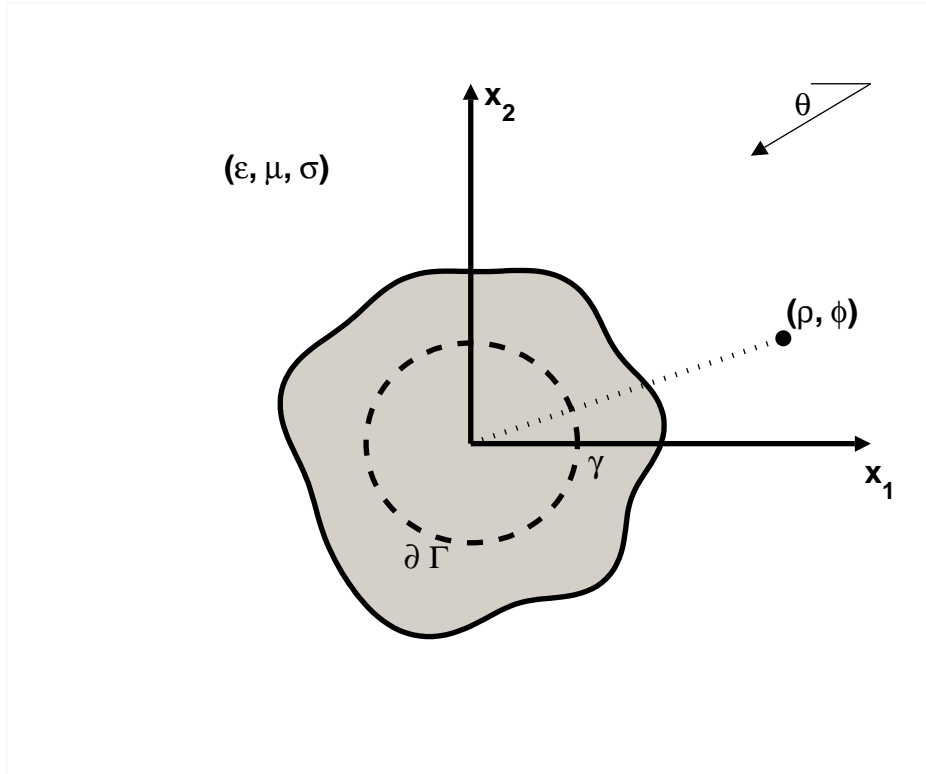
Figure 4.1: The problem geometry for the shape reconstruction method based on equivalent surface impedance modeling. γ: radius of the equivalent impedance circle.

distributions outside of D, the unknown surface impedance $\eta(x)$ can be determined from the measured far field of the actual scatterer.

It proves convenient to divide the problem into two parts. In the first part, a proper representation of the scattered field in the region external to the auxiliary object is determined. Later, the equivalent impedance which is obtained through such representation is exploited to retrieve the unknown surface. It should be noted that, in the first part the scattered waves are handled separately for each incidence, whereas in the second one they are exploited simultaneously.

As far as the first step is concerned, the single layer-potential representation provides a convenient way to model the scattered field from PEC target. In a similar way to the shape reconstruction method explained in chapter 3, a regularized single-layer potential inversion is exploited to determine an unknown surface potential density $\Psi_n(\mathbf{x})$ on the impedance circle. When the potential density on $|\mathbf{x}| = \gamma$ is reconstructed, the total field and the normal derivative of the total field can be evaluated by using the

jump conditions for single-layer potential (2.14) and (2.15).

$$u_n(\mathbf{x}) = u_n^i(\mathbf{x}) + \int_{\partial\Gamma} G(\mathbf{x},\mathbf{y})\Psi_n(\mathbf{y})\mathrm{d}s(\mathbf{y}), \quad \mathbf{x} \in \partial\Gamma \tag{4.4}$$

$$\frac{\partial u_n}{\partial n}(\mathbf{x}) = \frac{\partial u_n^i}{\partial n}(\mathbf{x}) + \int_{\partial\Gamma} \frac{\partial G(\mathbf{x},\mathbf{y})}{\partial n(\mathbf{x})}\Psi_n(\mathbf{y})\mathrm{d}s(\mathbf{y}) - \frac{1}{2}\Psi_n(\mathbf{x}), \quad \mathbf{x} \in \partial\Gamma \tag{4.5}$$

In principle, in view of (4.2) the surface impedance can be obtained from the values of the total field u_n and its normal derivative $\partial u_n/\partial n$ on $|\mathbf{x}| = \gamma$ via

$$\eta_n(\mathbf{x}) = -ik\frac{u_n(\mathbf{x})}{\dfrac{\partial u_n}{\partial n}(\mathbf{x})} \tag{4.6}$$

Possible zeros of the denominator on the right hand side of (4.6) are eliminated in the least squares sense and here and in the sequel, it is assumed that $\eta_n(\mathbf{x}) \neq 0$ for all $|\mathbf{x}| = \gamma$ [48, 51].

For the numerical evaluation of these singular integrals in (4.4) and (4.5), first they are parameterized as:

$$u_n(\phi) = e^{-ik\gamma\cos(\phi-\theta_n)} + \frac{i\gamma}{4}\int_0^{2\pi} H_0^{(1)}\left(2k\gamma\left|\sin\frac{\phi-\tau}{2}\right|\right)\Psi(\tau)\mathrm{d}\tau, \tag{4.7}$$

$$\frac{\partial u_n}{\partial\rho}(\phi) = -ik\cos(\phi-\theta_n)e^{-ik\gamma\cos(\phi-\theta_n)}$$
$$- \frac{ik\gamma}{2}\int_0^{2\pi}\left|\sin\frac{\phi-\tau}{2}\right|H_1^{(1)}\left(2k\gamma\left|\sin\frac{\phi-\tau}{2}\right|\right)\Psi(\tau)\mathrm{d}\tau - \frac{1}{2}\Psi(\phi) \tag{4.8}$$

then Nyström method which is later discussed in the next section is applied.

4.2 Reconstruction Algorithm

Since the surface impedance is determined through (4.6), the direct scattering problem related to the equivalent configuration in figure 4.1 can be solved in order to get the field in the exterior region $|\mathbf{x}| > \gamma$. The field calculated in the region between the impedance circle and the boundary of the unknown obstacle, is not physical, but it is identical to the one created by the original object in the region outside of the unknown object $\mathbb{R}^2 \setminus \overline{D}$.

The direct scattering problem related to the equivalent problem can be solved by applying Green's representation theorem [2]. The scattered field u^s has the following

24

representation in region $|\mathbf{x}| > \gamma$

$$u^s(\mathbf{x}) = \int_{\partial\Gamma} \left\{ u^s(\mathbf{y})\frac{\partial G(\mathbf{x},\mathbf{y})}{\partial n(\mathbf{y})} + \frac{\partial u^s}{\partial n}(\mathbf{y})G(\mathbf{x},\mathbf{y}) \right\} u^s(\mathbf{y})\mathrm{d}s(\mathbf{y}), \quad \mathbf{x} \in \mathbb{R}^2 \setminus \overline{\Gamma}. \tag{4.9}$$

Similarly, the incident field u^i is represented with [2, 48]

$$0 = \int_{\partial\Gamma} \left\{ u^i(\mathbf{y})\frac{\partial G(\mathbf{x},\mathbf{y})}{\partial n(\mathbf{y})} + \frac{\partial u^i}{\partial n}(\mathbf{y})G(\mathbf{x},\mathbf{y}) \right\} u^i(\mathbf{y})\mathrm{d}s(\mathbf{y}), \quad \mathbf{x} \in \mathbb{R}^2 \setminus \overline{\Gamma}. \tag{4.10}$$

By combining (4.9) and (4.10) together with (4.2), the following representation for the scattered field in term of single- and double-layer potentials is obtained

$$u^s(\mathbf{x}) = \int_{\partial\Gamma} \left\{ \frac{\partial G(\mathbf{x},\mathbf{y})}{\partial n(\mathbf{y})} + \frac{ik}{\eta(\mathbf{y})}G(\mathbf{x},\mathbf{y}) \right\} u(\mathbf{y})\mathrm{d}s(\mathbf{y}), \quad \mathbf{x} \in \mathbb{R}^2 \setminus \overline{\Gamma}. \tag{4.11}$$

Extending the representation to the boundary $\partial\Gamma$ by using the jump conditions given in (2.14) and (2.16) yields to the following singular integral equation.

$$u(\mathbf{x}) - 2\int_{\partial\Gamma} \left\{ \frac{\partial G(\mathbf{x},\mathbf{y})}{\partial n(\mathbf{y})} + \frac{ik}{\eta(\mathbf{y})}G(\mathbf{x},\mathbf{y}) \right\} u(\mathbf{y})\mathrm{d}s(\mathbf{y}) = 2u^i(\mathbf{x}), \quad \mathbf{x} \in \partial\Gamma \tag{4.12}$$

For the numerical treatment of this singular integral equation (4.12) and the integrals appearing in (4.4) and (4.5), Nyström method which takes proper care of the logarithmic singularity of the fundamental solution is used [52, 53]. In particular, with Nyström method a singular integral equation is divided into singular and non-singular parts. While the non-singular part is simply calculated with trapezoidal rule, the singular part is approximated with a special quadrature rule. Since the singular integrals in (4.12) are all defined on the boundary $\partial\Gamma$ which is a circle with radius γ, the required calculations are greatly simplified. Hence here the Nyström method is summarized in a form as it is applied to the integral equations in (4.12). Parameterizing $\mathbf{x}$ as

$$x(\phi) = (\gamma\cos\phi, \gamma\sin\phi), \quad \phi \in [0, 2\pi) \tag{4.13}$$

yields the following parameterized integral equation for (4.12)

$$v(\phi) - \int_0^{2\pi} K(\phi, \tau)v(\tau)\mathrm{d}\tau = g(\phi), \tag{4.14}$$

where $v(\phi) = u(x(\phi))$ and $g(\phi) = -2u^i(x(\phi))$. The kernel of (4.14) can be written as

$$K(\phi, \tau) = L(\phi, \tau) + \frac{i}{\eta(\tau)}M(\phi, \tau) \tag{4.15}$$

where $L(\phi, \tau)$ and $M(\phi, \tau)$ is given by

$$L(\phi, \tau) = \frac{ik\gamma}{2} \left| \sin \frac{\phi - \tau}{2} \right| H_1^{(1)} \left(2k\gamma \left| \sin \frac{\phi - \tau}{2} \right| \right) \tag{4.16}$$

$$M(\phi, \tau) = \frac{ik\gamma}{2} H_0^{(1)} \left(2k\gamma \left| \sin \frac{\phi - \tau}{2} \right| \right) \tag{4.17}$$

Both $L(\phi, \tau)$ and $M(\phi, \tau)$ can be separated into singular and non-singular parts as such

$$L(\phi, \tau) = L_1(\phi, \tau) \ln \left(4 \sin^2 \frac{\phi - \tau}{2} \right) + L_2(\phi, \tau) \tag{4.18}$$

$$M(\phi, \tau) = M_1(\phi, \tau) \ln \left(4 \sin^2 \frac{\phi - \tau}{2} \right) + M_2(\phi, \tau) \tag{4.19}$$

where

$$L_1(\phi, \tau) = -\frac{k}{2\pi} \left| \sin \frac{\phi - \tau}{2} \right| J_1 \left(2k\gamma \left| \sin \frac{\phi - \tau}{2} \right| \right) \tag{4.20}$$

$$L_2(\phi, \tau) = L(\phi, \tau) - L_1(\phi, \tau) \ln \left(4 \sin^2 \frac{\phi - \tau}{2} \right) \tag{4.21}$$

$$M_1(\phi, \tau) = -\frac{\gamma}{2\pi} J_0 \left(2k\gamma \left| \sin \frac{\phi - \tau}{2} \right| \right) \tag{4.22}$$

$$M_2(\phi, \tau) = M(\phi, \tau) - M_1(\phi, \tau) \ln \left(4 \sin^2 \frac{\phi - \tau}{2} \right) \tag{4.23}$$

The diagonal terms further simplifies to:

$$L_2(\phi, \phi) = L(t, t) = \frac{1}{2\pi} \tag{4.24}$$

$$M_2(\phi, \phi) = \frac{\gamma}{\pi} \left\{ \frac{i\pi}{2} - C - \ln \left(\frac{k\alpha}{2} \right) \right\} \tag{4.25}$$

As seen in above equations, the logarithmic singularity of the fundamental solution is separated as in the form of $\ln \left(4 \sin^2 \frac{\phi - \tau}{2} \right)$. Later integrals regarding to this singular part is approximated with the quadrature rule for an equidistant set of nodes $\phi_n = \frac{\pi}{N} n$, $n = 0, ..., 2N - 1$

$$\int_0^{2\pi} \ln \left(4 \sin^2 \frac{\phi - \tau}{2} \right) f(\tau) d\tau \approx \sum_{n=0}^{2N-1} R_n^{(N)}(\phi) f(\phi_n), \quad 0 \le \phi \le 2\pi \tag{4.26}$$

with the quadrature weights given as [2]:

$$R_n^{(N)}(\phi) = -\frac{2\pi}{N} \sum_{m=1}^{N-1} \frac{1}{m} \cos(m(\phi - \phi_n)) - \frac{\pi}{N^2} \cos(N(\phi - \phi_n)), \quad n = 0, ..., 2N - 1 \tag{4.27}$$

26

and the non-singular parts are calculated through trapezoidal rule:

$$\int_0^{2\pi} f(\tau)\mathrm{d}\tau = \frac{\pi}{N}\sum_{n=0}^{2N-1} f(\phi_n) \tag{4.28}$$

Consequently, the integral equation (4.14) is replaced with the approximating equation

$$v^{(N)}(\phi) - \sum_{n=0}^{2N-1}\left\{R_n^{(N)}(\phi)K_1(\phi,\phi_n) + \frac{\pi}{N}K_2(\phi,\phi_n)\right\}v^{(N)}(\phi_n) = g(t) \tag{4.29}$$

By further discretizing $v_m^{(N)} = v^{(N)}(\phi_m)$, $m = 0,1,...,2N-1$, the solution of (4.29) is reduced to finite dimensional linear system of equations

$$v_m^{(N)} - \sum_{n=0}^{2N-1}\left\{R_{|m-n|}^{(N)}K_1(\phi_m,\phi_n) + \frac{\pi}{N}K_2(\phi_m,\phi_n)\right\}v_n^{(N)} = g(\phi_m), \quad m = 0,1,...,2N-1 \tag{4.30}$$

where

$$R_x^{(N)} = -\frac{2\pi}{N}\sum_{n=1}^{N-1}\frac{1}{n}\cos(\frac{nx\pi}{N}) - \frac{(-1)^x\pi}{N^2}, \quad x = 0,1,...,2N-1 \tag{4.31}$$

Once the resulting system of linear equation is solved, the scattered field u_n^s for each illumination is calculated through (4.11). With the knowledge of the total field, the unknown shape ∂D can be reconstructed by searching the points where the total field for each experiment vanishes according to the boundary condition (2.5), which yields:

$$\begin{aligned}F_1(f) &= 0\\ &\vdots\\ F_N(f) &= 0\end{aligned} \tag{4.32}$$

where $F_n(f)$ are the nonlinear operator corresponding to n'th measurement and is explicitly given by

$$\begin{aligned}F_n(f(\phi)) &= e^{-ikf(\phi)\cos(\phi-\theta_n)}\\ &+ \frac{ik\gamma}{4}\int_0^{2\pi}\left\{\frac{f(\phi)-\gamma\cos(\phi-\tau)}{|R|}H_1^{(1)}(k|R|) + \frac{i}{\eta(\tau)}H_0^{(1)}(k|R|)\right\}u_n(\tau)\mathrm{d}\tau\end{aligned} \tag{4.33}$$

where

$$R = \sqrt{f^2(\phi) + \gamma^2 - 2f(\phi)\gamma\cos(\phi-\tau)}. \tag{4.34}$$

Thus the shape reconstruction problem is reduced to the solution of a set of nonlinear equations (4.32) for the unknown function $f(\phi)$. To solve (4.32), the Gauss-Newton

algorithm which is previously explained in section 3.4 is exploited. Briefly, (4.32) is first linearized in Newton sense as in (3.15) where the Fréchet derivative F' is explicitly given by:

$$F'_n(f(\phi)) = -ik\cos(\phi - \theta_n)e^{-ikf(\phi)\cos(\phi - \theta_n)} +$$
$$\frac{ik\gamma}{4}\int\limits_0^{2\pi}\left(A_0 H_0^{(1)}(kR) + A_1 H_1^{(1)}(kR)\right)\Psi(\tau)d\tau \tag{4.35}$$

where

$$A_0 = \frac{k(-\rho + \gamma\cos(\tau - \phi))(\gamma - \rho\cos(\tau - \phi))}{R^2} \tag{4.36}$$

and

$$A_1 = i\frac{\left(-kR^2(\rho - \gamma\cos(\tau - \phi)) + i\left(-2\gamma\rho + \left(\gamma^2 + \rho^2\right)\cos(\tau - \phi)\right)\eta(\tau)\right)}{R^3\eta(\tau)} \tag{4.37}$$

The difference Δf which updates the reconstructed shape at each iteration is expanded into a series (3.17) to search for a finite dimensional solution in order to reduce instabilities. Thus the resulting system of linear equations are given as

$$\begin{bmatrix} F'_1\vartheta_1(\phi) & F'_1\vartheta_2(\phi) & \cdots & F'_1\vartheta_P(\phi) \\ F'_2\vartheta_1(\phi) & F'_2\vartheta_2(\phi) & \cdots & F'_2\vartheta_P(\phi) \\ \vdots & \vdots & & \vdots \\ F'_N\vartheta_1(\phi) & F'_N\vartheta_2(\phi) & \cdots & F'_N\vartheta_P(\phi) \end{bmatrix}\begin{bmatrix} a_1 \\ a_2 \\ \vdots \\ a_P \end{bmatrix} = -\begin{bmatrix} F_1 \\ F_2 \\ \vdots \\ F_N \end{bmatrix} \tag{4.38}$$

which can be written in a compact form as follows:

$$\mathbf{J}_F(f_i)\mathbf{x}_{i+1} = -\mathbf{V}(f_i), \tag{4.39}$$

Later the least squares solution is achieved by iterating

$$\mathbf{x}_{i+1} = -\left[\mathbf{J}_F^*(f_i)\mathbf{J}_F(f_i)\right]^{-1}\mathbf{J}_F^*(f_i)\mathbf{V}(f_i). \tag{4.40}$$

until the inequality $||x_{i+1} - x_i|| < \delta$ is satisfied for a predefined threshold δ.

5. NUMERICAL RESULTS

Two analytical continuation based shape reconstruction methods for inaccessible, perfect electric conductors are presented in chapter 3 and chapter 4. Here, numerical validations of the presented methods are addressed. To this aim, several numerical simulations are performed in order to reveal both capabilities and the limitations of the methods. Moreover, by using the same problem configurations, methods are compared by means of the accuracy and the numerical efficiency. The quality of the reconstructions is quantified with the reconstruction error *err* defined as:

$$err = \frac{||f - \tilde{f}||}{||f||} = \sqrt{\frac{\sum_n |f(\phi_n) - \tilde{f}(\phi_n)|^2}{\sum_n |f(\phi_n)|^2}} \tag{5.1}$$

where $\tilde{f}$ denotes the estimated shape.

As noted before, only starlike, smooth boundaries with parametric representations

$$\partial D := \{(x_1(\phi), x_2(\phi)) : \phi \in [0, 2\pi)\} \tag{5.2}$$

are considered for the numerical simulations. The far field data is synthetically generated by solving the associated direct scattering problem through a mixed representation of single- and double-layer potentials [33]. By using the jump conditions on the boundary, the direct problem is transformed into the solution of a singular integral equation which is again handled with the Nyström method outlined in section 4.2. In all simulations, the far field pattern is sampled at total $T = 60$ equiangular points and a random noise term is added to the sampled far field data as:

$$\tilde{u}^\infty(\hat{x}) = u^\infty(\hat{x}) + \xi |u^\infty(\hat{x})| e^{i2\pi r_u}, \tag{5.3}$$

where $\xi > 0$ is noise level and r_u is uniformly distributed random variable between $[0, 1)$, to assure the stability of the reconstructions. In this case, the corresponding signal-to-noise ration is $SNR = -20 \log_{10} \xi$.

In the application of the least square solution (3.17), the basis functions are chosen as

$$\vartheta_p(\phi) = e^{-ip\phi}, \quad p = 0, \pm 1, ... \pm P, \tag{5.4}$$

which in turn, means the expansion of the unknown function to a Fourier series. As the Fourier series is truncated for numerical evaluation, the estimated shape becomes smoothed replica of the exact shape.

5.1 Numerical Result for the Method Based on Analytical Continuation of the Scattered Field Through Taylor Series Expansion

Before advancing into numerical result, here the details of numerical implementation will be discussed. The method is quite suitable for vectorization, thus it is possible to write quite fast programs implementing the method. In fact, each of the simulations performed in rest of this section took less than 5 seconds on a standard PC. One major problem in numerical implementation is calculation of the derivatives in (3.11). It is not possible to simplify them in a straightforward manner, thus symbolic computation techniques are used for numerical evaluation. The complexity of the derivatives increases nonlinearly as the order M increases. Since it is not proven that the Taylor series expansion of the scattered field (3.8) is always convergent to the surface, for practical purposes, the order M of the derivatives is limited to 5 or less in the simulations. It should be noted that one can attempt to take advantage of the addition theorem

$$H_0^{(1)}\left(k\sqrt{\rho^2 + \alpha^2 - 2\alpha\rho\cos(\phi - \tau)}\right) = \sum_{n=-\infty}^{\infty} J_n(k\rho)H_n^{(1)}(k\alpha)e^{in(\phi - \tau)}, \quad \rho < \alpha$$

(5.5)

by truncating the series for the numerical evaluation. In this case it is possible to take the derivatives in a simple manner [34]

$$\frac{\partial^M J_n(k\rho)}{\partial\rho^M} = (\frac{k}{2})^M \sum_{m=0}^{M} (-1)^m \binom{M}{m} J_{n-M-2m}(k\rho).$$

(5.6)

Although this approach approximates lower order terms with a reasonable accuracy, it does not converge sufficiently fast to higher order derivatives. Thus it is not suitable for numerical evaluation of the derivatives in (3.11).

As a first example, an object whose boundary ∂D_1 is given by the normalized parametric equation

$$x_1/\lambda = 0.2(\cos\phi + 0.2\cos 3\phi)$$
$$x_2/\lambda = 0.2(\sin\phi + 0.2\cos 3\phi),$$

(5.7)

is considered. The object is illuminated by a time harmonic, plane wave with incidence angle $\theta_1 = 0$ at $f = 300$MHz. A random noise with $\xi = 0.01$ is added to the far field pattern, thus $SNR = 40dB$. In order to demonstrate how the proposed approach works, in this example it is assumed that the radius of the minimum circle $\alpha = 0.25\lambda$ is known a priori.

The first part of the method is concerned with the reconstruction of the scattered field in the vicinity of the object from the knowledge of the noisy far field pattern. To apply the TSVD inversion method described in section 3.2, it is needed to choose a proper regularization parameter R. Before advancing into details of the method, here the selection of regularization parameter is discussed. In figure 5.1 general behavior of singular values is shown. As it can be observed, the singular values of the far field equation (3.3) are grouped as pairs and rapidly decays. As a result of the ill-posedness of the underlying problem, the discretized version of (3.2) becomes ill-conditioned. For this example the condition number is $\kappa = 5.9244 \times 10^{16}$ and it is not possible to calculate the correct inversion of the system of linear equations without improving its condition number. By truncating the singular values and their corresponding singular
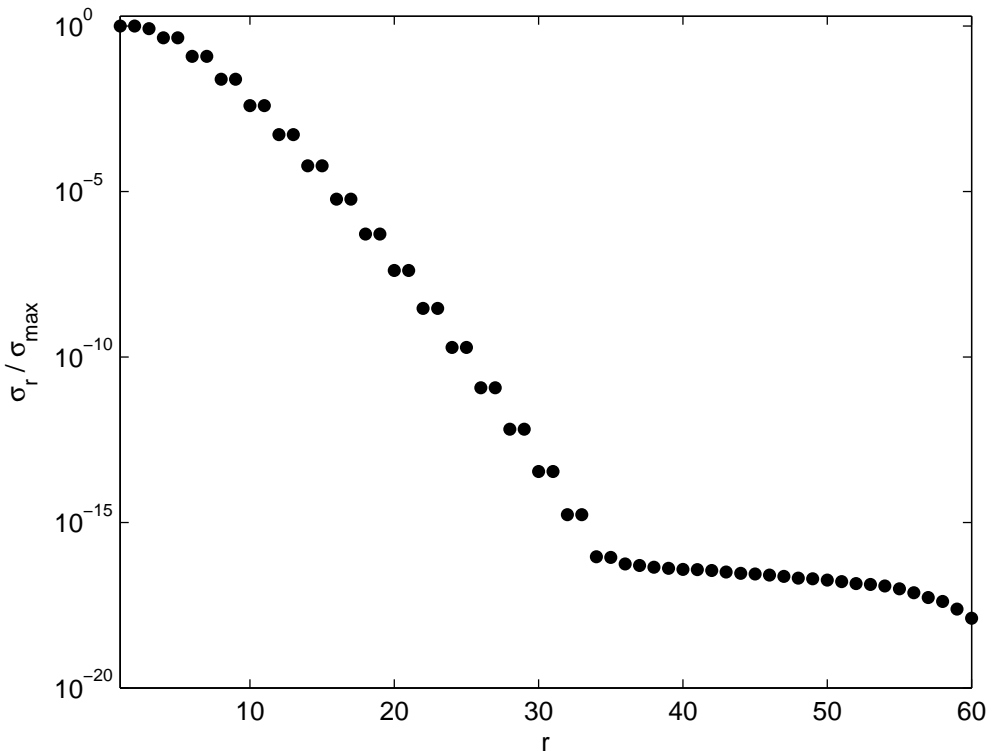

Figure 5.1: Variation of the normalized singular values in the TSVD inversion of the far field equation

31

vectors, the higher order singular values are discarded. As a result, the regularized matrix shares the same characteristics such as having the same matrix norm but it is better conditioned so that it is possible to numerically evaluate the inversion. Moreover by discarding the higher order singular values, the noise on the data is filtered to some extent since the higher order singular values are more likely to be corrupted.

To select a proper regularization parameter R, as described in section 3.2, the Morozov's discrepancy principle is utilized [37]. Figure 5.2 depicts how the optimal parameter is selected. By plotting $||S\Psi^{(r)} - u^\infty||$ in logarithmic scale, the index of the first singular value of which the values is smaller than the predetermined threshold is selected. For this example R is selected as 9. The major disadvantage of this approach is that in order to determine the threshold, an estimate of the noise power is needed, but such an estimate may not be available in practical cases. Another possible method which does not require the estimate of noise power is so called "L-curve" approach [54]. By plotting $||S\Psi^{(r)} - u^\infty||$ vs $||\Psi^{(r)}||$ in a logarithmic scale, generally a L-shaped plot appears. The regularization parameter is the index of the singular value which is on the corner of the L-curve. In figure 5.3, the plot of L-curve is shown. Here again the truncation index is chosen as $R = 9$.

When the regularization parameter is fixed, by inverting (3.2) the single layer potential density is solved. In figure 5.4 the variation of the amplitude and the phase of the reconstructed single-layer potential density $\Psi^{(R)}(\tau)$ are shown. As a result of the symmetry in the problem configuration, $\Psi^{(R)}(\tau)$ is symmetrical as well. To confirm the effectiveness of the single-layer potential inversion, the scattered field on the circle $\beta = 0.3\lambda$ is calculated by the use of reconstructed single-layer potential density. Figure 5.5 shows the comparisons between the amplitudes and the phases of the exact and the reconstructed scattered field values, respectively. As it can be observed, the regularized analytical continuation through single-layer potential approach yields a very accurate result for the phase, while the reconstructed amplitude is slightly affected by the approximation introduced by the TSVD. In any case, it appears that the method provides a good approximation of the scattered field, even in presence of noise on data. This is a very important point, as the reconstruction algorithm given in section 3.3 exploits the knowledge of the scattered field and its derivatives on the circle $\rho = \beta$. As these required values are calculated through the analytical continuation of the
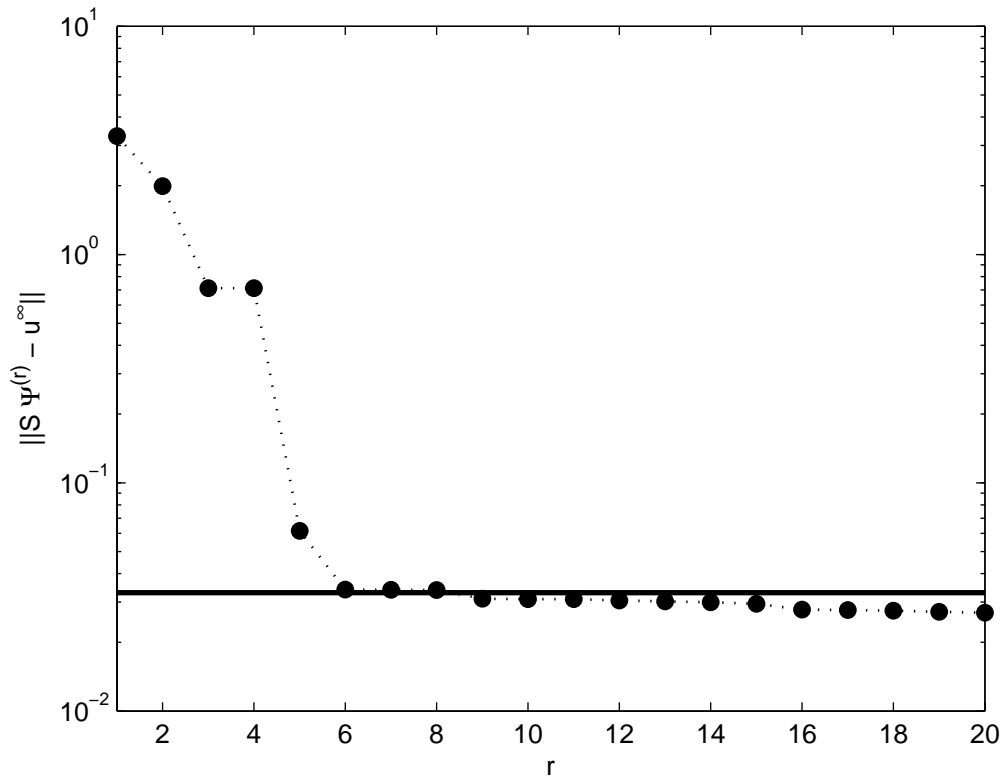
Figure 5.2: Selection of the regularization parameter for TSVD inversion by using Morozov's discrepancy principle
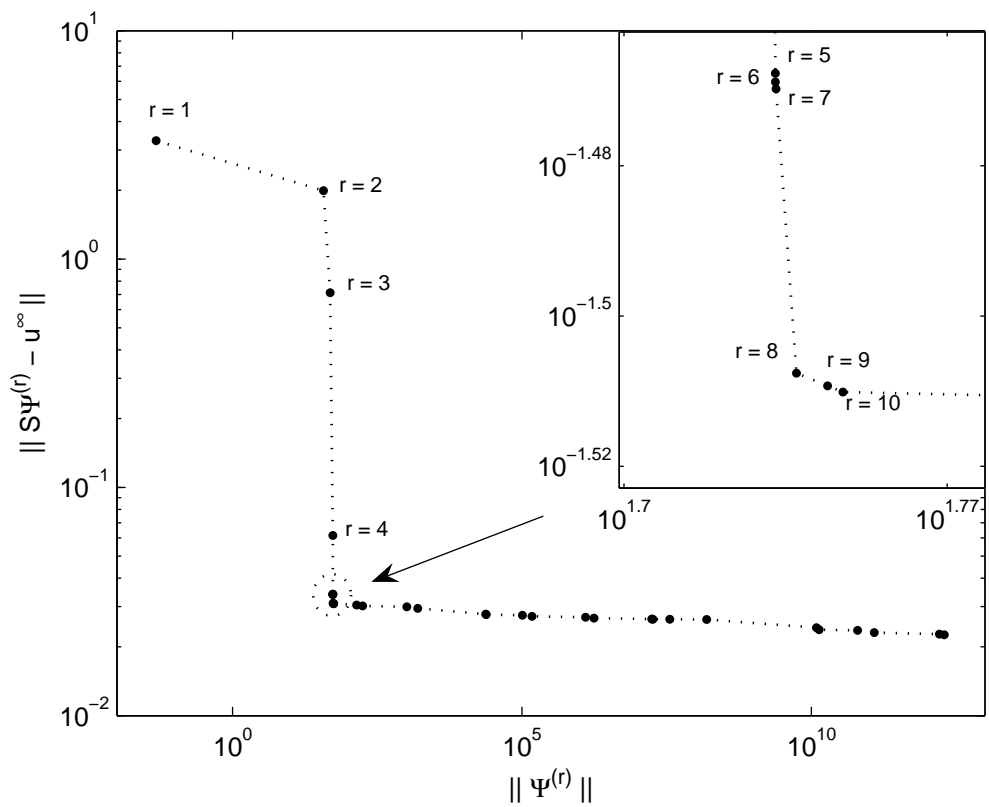
Figure 5.3: Selection of the regularization parameter for TSVD inversion by using L-Curve approach
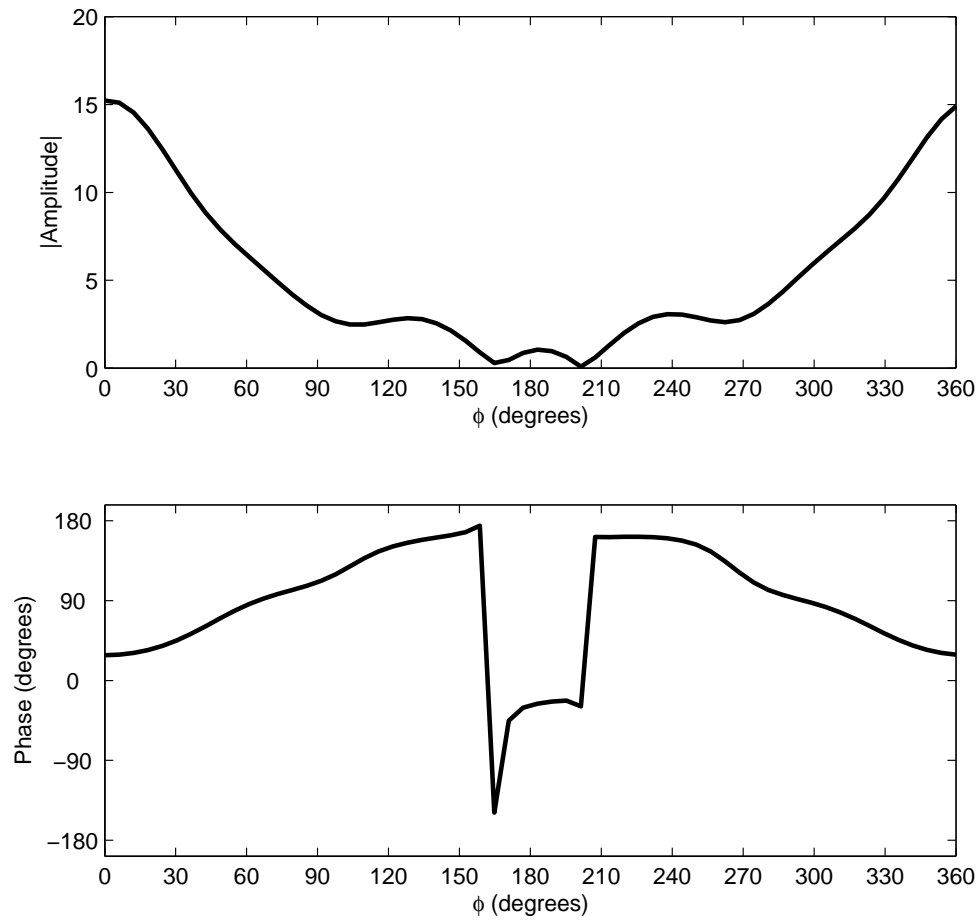
Figure 5.4: The amplitude and the phase of the reconstructed single-layer potential density

measured data to the minimum circle, the overall performance of the method is closely related to the accuracy of the reconstructed field.

In the second step of the method, the estimated field is used to build the nonlinear functional (3.13) and the Newton minimization is performed. Figure 5.6 illustrates the exact and reconstructed shapes. As it can be observed, it yields to be a very accurate reconstruction. Here, the number of terms in the Taylor expansion is $M = 3$, the minimum circle is used as the starting guess and the number of basis functions is $P = 9$.

The shape of the target in the first example is simple and only single illumination is enough to achieve satisfactory reconstruction. In order to reveal the behavior of the method in the case of complex shapes, an object with parametric boundary ∂D_2 given
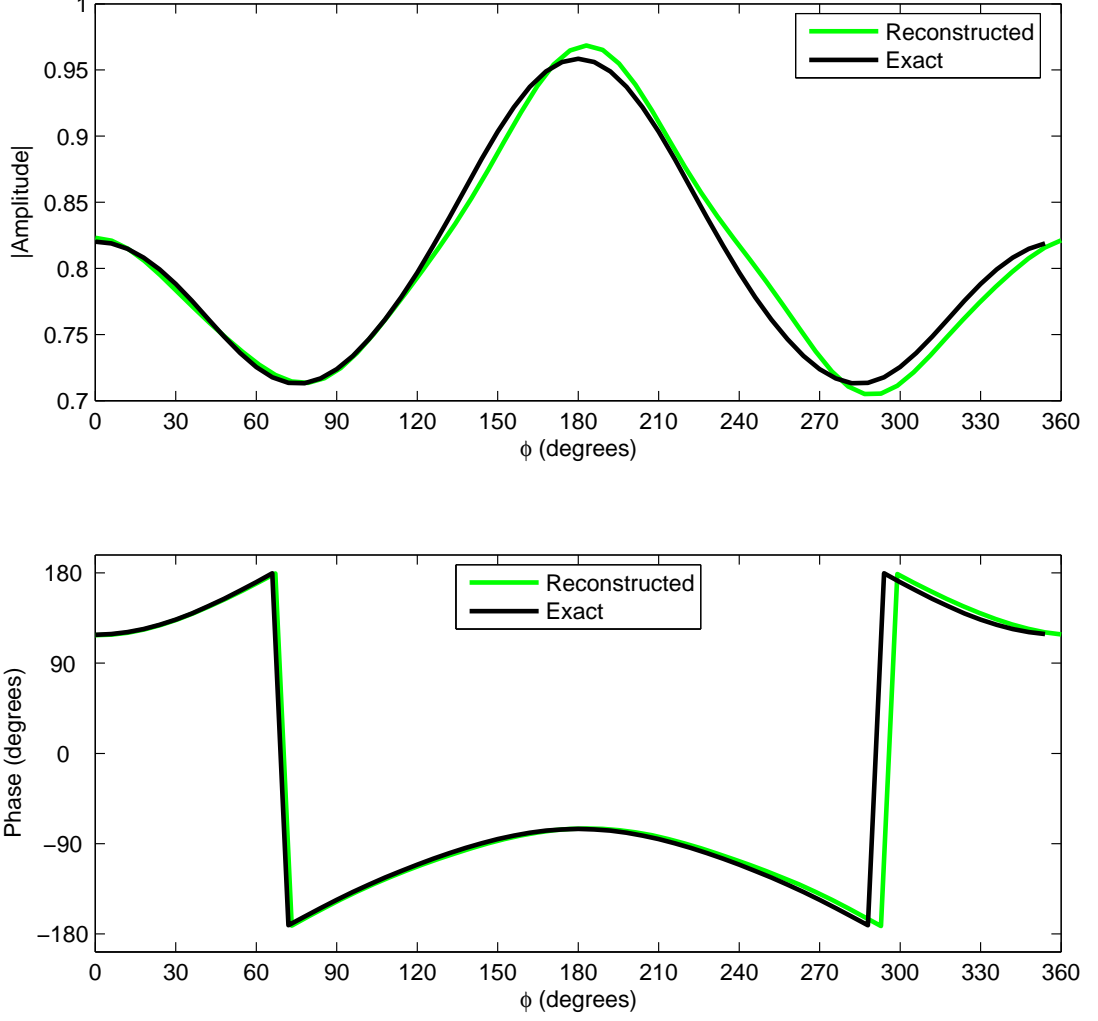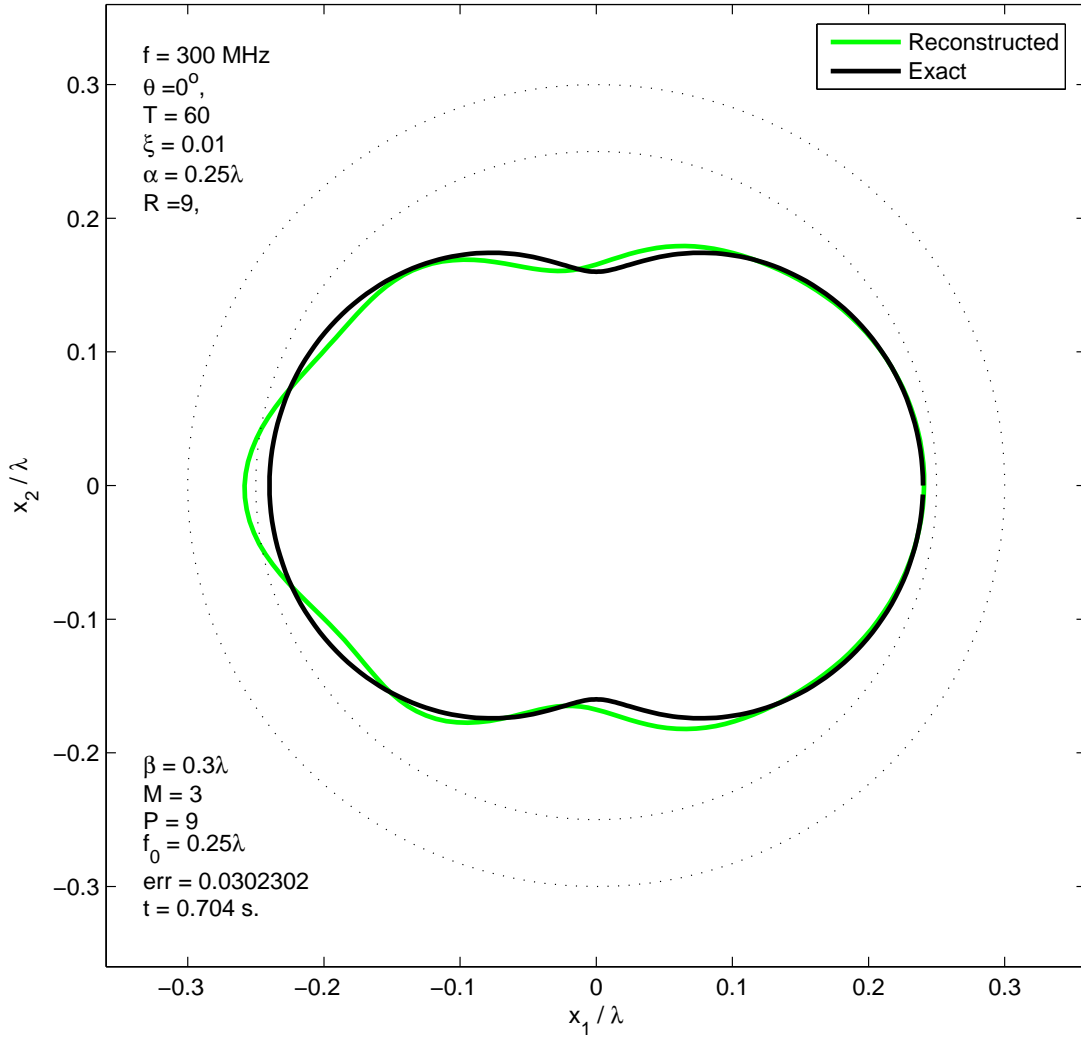
Figure 5.5: Comparison of the reconstructed and the actual scattered fields on a circle with radius $\rho = \beta = 0.3\lambda$.

by

$$x_1/\lambda = 0.48\cos\phi + 0.20\cos 2\phi - 0.12$$

$$x_2/\lambda = 0.48\sin\phi, \quad \phi \in [0, 2\pi].$$

(5.8)

which has quite apparent convex and concave regions is considered. The object is illuminated with a set of plane waves with incident angles $\theta_1 = 0, \theta_2 = \frac{\pi}{2}, \theta_3 = \pi$ and $\theta_4 = \frac{3\pi}{2}$ at $f = 600\text{MHz}$. A random term with $\xi = 0.0316$ (SNR = 30dB) is added to the simulated data. Here it is assumed that a good estimate about the size of the target is available so the radius of the minimum circle is selected as $\alpha = 0.64\lambda$ while $\beta = 0.80\lambda$. Other simulation parameters are $M = 4$ and $P = 9$. The reconstructed shapes are shown in figure 5.7(a), figure 5.7(b) and figure 5.7(c) for the incidence directions $\theta_1 = 0$, $\theta_2 = \frac{\pi}{2}$ and $\theta_3 = \pi$, respectively. It is observed that the method provides quite accurate reconstructions on the illuminated side but the quality of the

Figure 5.6: Comparison of exact and reconstructed shapes of the object given by the boundary ∂D_1 with a single illumination.

reconstructions degrades gradually on the unilluminated side depending on the noise level and the complexity of the unknown shape. In order to demonstrate the effects of the multiview configuration on the quality of reconstructions, two illuminations in the opposite directions are considered and successful reconstructions are obtained for the illuminations with $\theta_1 = 0$ and $\theta_3 = \pi$ in figure 5.7(d), and for the illuminations with $\theta_2 = \frac{\pi}{2}$ and $\theta_4 = \frac{3\pi}{2}$ in figure 5.7(e). The last simulation for this example is performed for the case the object is illuminated in four directions and the result is shown in figure 5.7(f). As the reconstruction in figure 5.7(f) is not superior as compared to simulations with two opposite incidence directions, it is concluded that there is an upper limit on how much the reconstruction quality can be improved by introducing multiview data. The third example is dedicated to show how the selection of minimum circle affects the quality of the reconstructions. Since the method uses Taylor series expansion
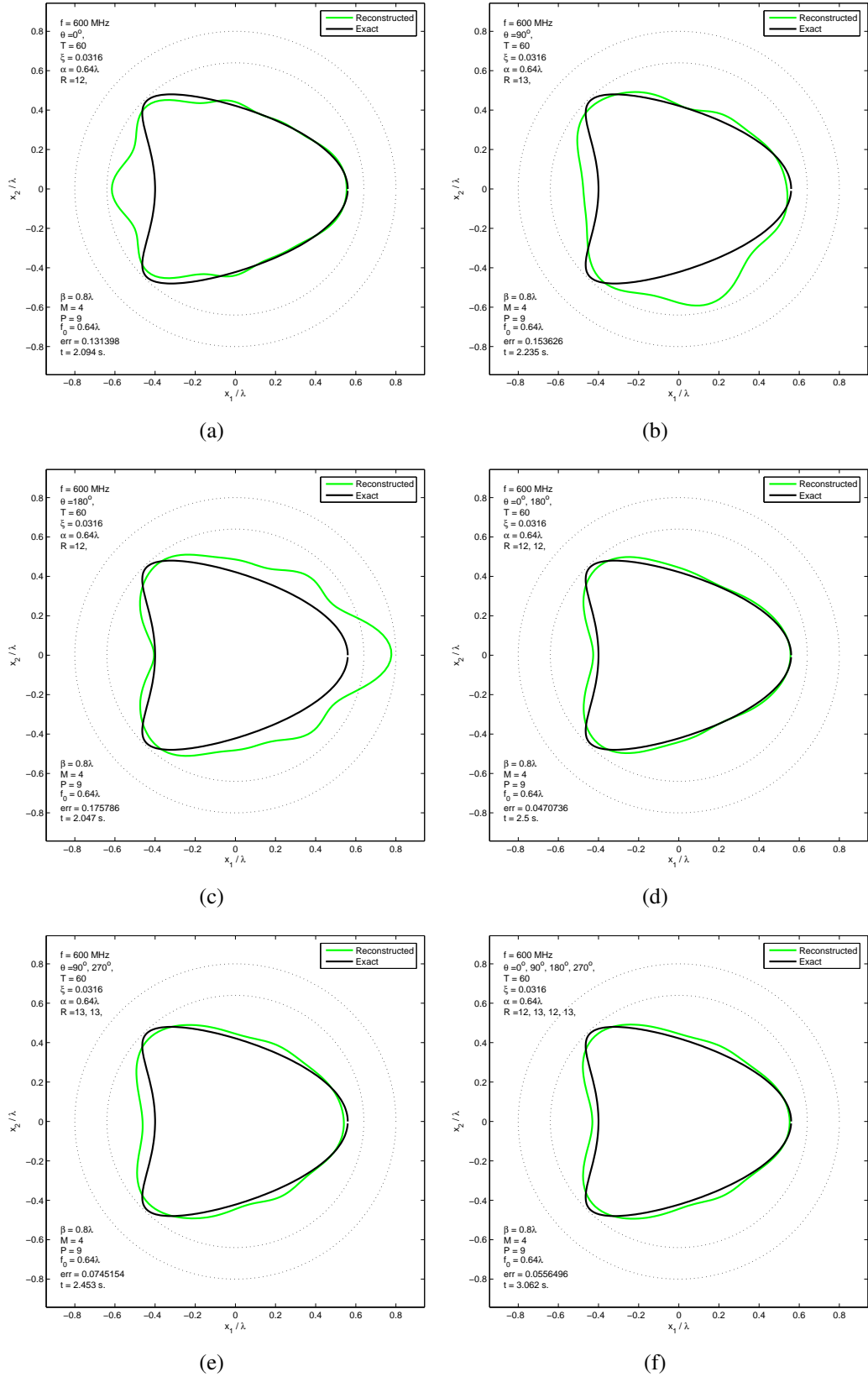
Figure 5.7: Comparison of the exact and the reconstructed shapes of the object with the boundary ∂D_2 for different incidence directions $\theta_1 = 0, \theta_2 = \frac{\pi}{2}, \theta_3 = \pi$ and $\theta_4 = \frac{3\pi}{2}$. (a) θ_1, (b) θ_2, (c) θ_3, (d) θ_1 and θ_3 (e) θ_2 and θ_4 (f) $\theta_1, \theta_2, \theta_3$ and θ_4
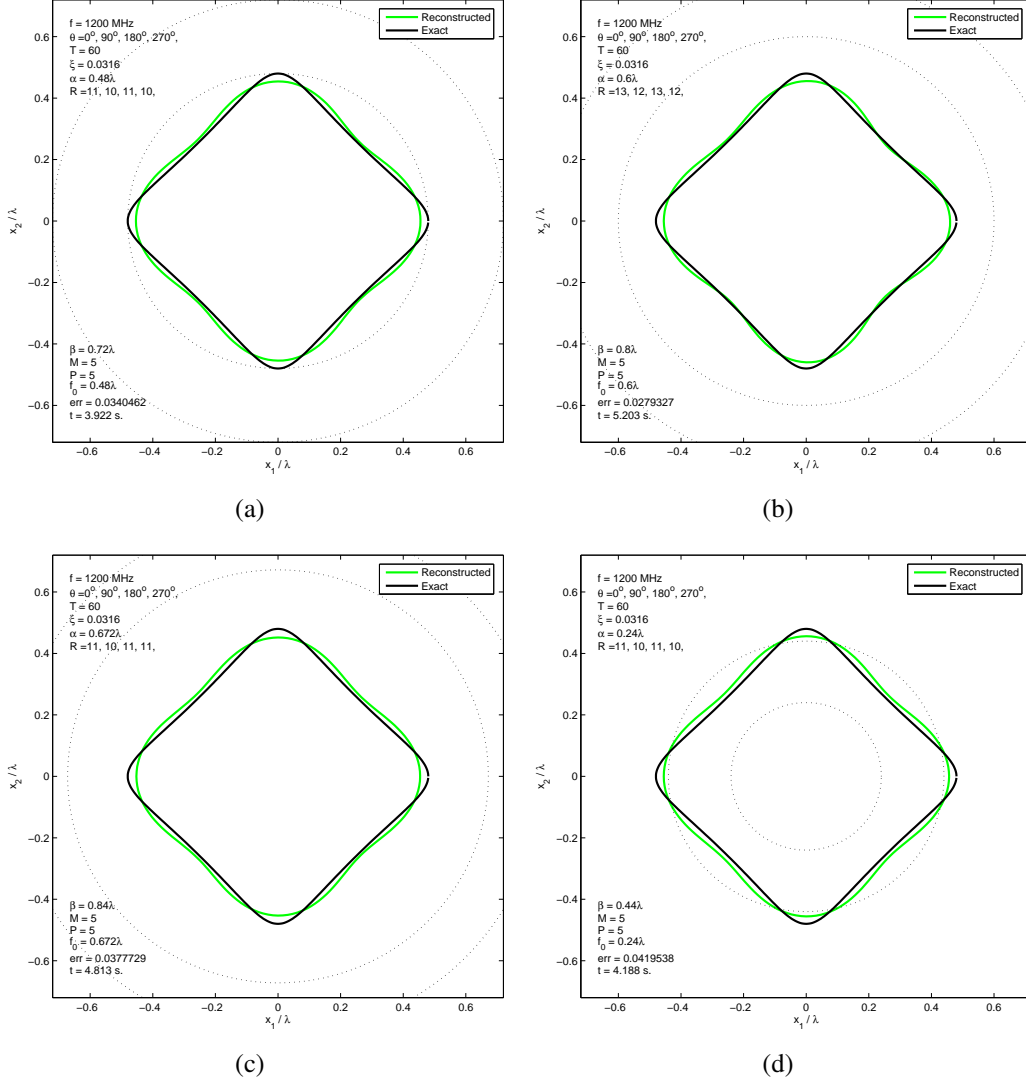
Figure 5.8: Comparison of the exact and reconstructed shapes of the object with the boundary ∂D_3 for different estimation of the radius of the minimum circle. (a) $\alpha = 0.48\lambda$ (exact) (b) $\alpha = 0.6\lambda$ (c) $\alpha = 0.672\lambda$ (d) $\alpha = 0.24\lambda$

of the reconstructed field, the distance $\frac{|f(\phi) - \beta|}{\lambda}$ should be small so proper selection of the radius of minimum circle α is important for computational purposes. In the open literature, there are proposed method for estimating the convex hull of the target [55, 56]. The method presented in [56] estimates the radius of minimum circle as $\Delta W = 2k\alpha$ where the spatial bandwidth ΔW is determined through the Fourier analysis of the scattered field. However it is reported that the approach works better for electrically large objects [56] while the estimate is generally larger than actual radius for electrically small objects [13]. Instead of attempting to estimate the minimum circle, here the main focus is to determine the limitations of the method depending on the radius of minimum circle. To this aim, a rounded square whose parametric
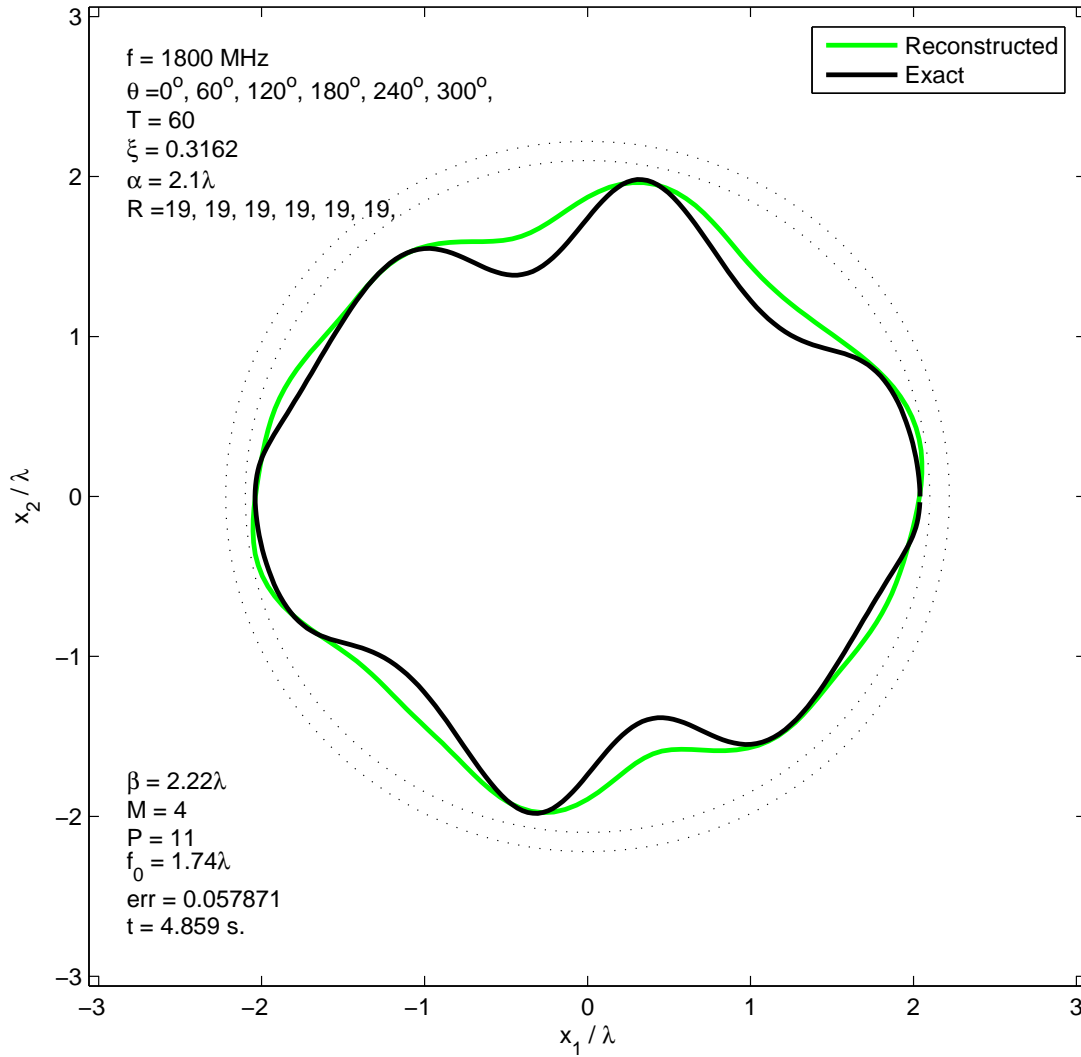
boundary ∂D_3 is given by

$$x_1/\lambda = 0.24(\cos^3\phi + \cos\phi)$$
$$x_2/\lambda = 0.24(\sin^3\phi + \sin\phi)$$

(5.9)

is considered. The object is illuminated with four different incident angles $\theta_1 = 0, \theta_2 = \frac{\pi}{2}, \theta_3 = \pi$ and $\theta_4 = \frac{3\pi}{2}$ at $f = 1200\text{MHz}$. Other simulation parameters are $P = 5, f_0 = \alpha, M = 5$ and $\xi = 0.0316$ (SNR = 30dB). The reconstructed shape with a correct minimum circle $\alpha = 0.48\lambda$ is shown in figure 5.8(a). Other parameters are $\beta = 0.72\lambda, R_1 = 11, R_2 = 10, R_3 = 11, R_4 = 10$. Although the method is unable to catch the corners exactly, the reconstruction is very successful. The reconstruction shown in figure 5.8(b) is produced for the parameters $\alpha = 0.6\lambda, \beta = 0.8\lambda, R_1 = 12, R_2 = 13, R_3 = 12, R_4 = 13$. In this case, while the estimated minimum circle is 25% larger than previous simulation, the reconstruction is still very accurate. The same simulation was repeated for larger estimates of the minimum circle and it was observed that, for this example, the reconstructions become unreliable when the estimates are around 50% or larger than the exact radius. In figure 5.8(c) the simulation with a 40% larger minimum circle is shown. The simulation parameters are $\alpha = 0.672\lambda, \beta = 0.84\lambda, R_{1,2,3,4} = 11$ and the reconstruction error is comparable to previous results. The last simulation for this example is performed when the radius is underestimated. The reconstruction in figure 5.8(d) is produced for the parameters $\alpha = 0.24\lambda, \beta = 0.44\lambda, R_1 = 11, R_2 = 10, R_3 = 11, R_4 = 10$. From these figures, it is concluded that the method can tolerate the variation of the radius of the minimum circle.

The sizes of the targets in previous examples are all smaller or comparable to the wavelength. Hence, as a last example, a larger object in terms of the wavelength whose boundary is given with the parametric equation

$$x_1/\lambda = (1.74 + 0.3\cos 2\phi)\cos\phi$$
$$x_2/\lambda = (1.74 + 0.3\sin 6\phi)\sin\phi$$

(5.10)

is considered. The object is illuminated at $f = 1800\text{MHz}$ with six different incidence angles $\theta_1 = 0, \theta_2 = \frac{\pi}{3}, \theta_3 = \frac{2\pi}{3}, \theta_4 = \pi, \theta_5 = \frac{4\pi}{3}$ and $\theta_6 = \frac{5\pi}{3}$. The simulated data is corrupted with a higher noise level $\xi = 0.316$ ($SNR = 10dB$) as compared to previous examples. The simulation parameters are $\alpha = 2.1\lambda$, $\beta = 2.22\lambda$, $R_{1,2...,6} = 19$ and $P = 11$. The reconstructed shape is shown in figure 5.9. For this simulation selecting

Figure 5.9: Comparison of the exact and reconstructed shapes of the object given by the boundary ∂D_4.

initial guess equal to the estimated minimum circle does not work, so the initial guess is chosen as $f_0 = 1.74\lambda$. Here it should be noted that since the method is quite fast, it is possible to repeat the simulation with different initial guesses to check the validity of the reconstruction. With this example, it is concluded that the usage of multiview data enables to reconstruct larger shapes in terms of wavelength. Besides, angle diversity enhances the robustness against noise.

As a final remark, let us note that, in order to avoid the solution of the nonlinear equation (3.20), one could consider to "directly" obtain the reconstruction of the unknown shape by simply plotting the total field as given by (3.8) inside the minimum circle and observing points where this field vanishes. Unfortunately, such a simple

strategy is not effective as it is not able to provide any reconstruction of the boundary of the object in the shadow region.

5.2 Numerical Results for the Method Based on Inhomogeneous Surface Impedance Modeling

Here, the simulations performed in the previous section are repeated with same noisy far field pattern for the method based on inhomogeneous surface impedance modeling, explained in chapter 4. This enables direct comparison of the methods as well as numerical validation of the impedance modeling based method.

Analogously, the first example is devoted to demonstrate how the surface impedance modeling based method works. Here the boundary defined in (5.7) is considered with the same source configuration. The real and the imaginary parts of the reconstructed
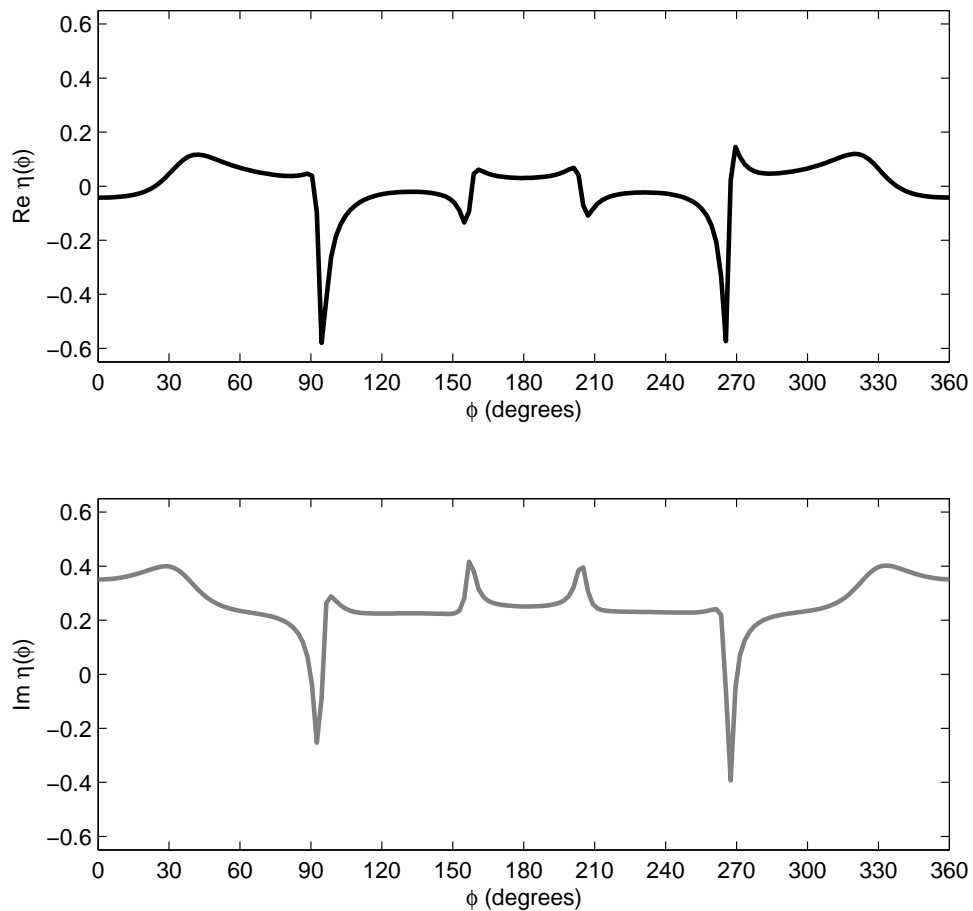
Figure 5.10: Real and imaginary parts of the reconstructed, normalized surface impedance

surface impedance $\eta(\phi)$ on a circle with radius $\gamma = 0.15\lambda$ are shown in figure 5.10. Due to the symmetry in the problem geometry in the illumination direction, a symmetry in the reconstructed $\eta(\phi)$ is apparent as well. Later in figure 5.11 the amplitude and the phase of the reconstructed scattered field on a circle with radius 0.3λ is shown. This result is quite similar to what is achieved with the first method in figure 5.5.

To validate the reasoning of modeling the unknown target with an inhomogeneous surface impedance, the 2D spatial variations of the total field is plotted in figure 5.12. As it is observed the variation of the total field which is calculated by using the reconstructed surface impedance discloses a rough sketch of the unknown target but the sketch becomes indistinguishable at the unilluminated side. However the sketch
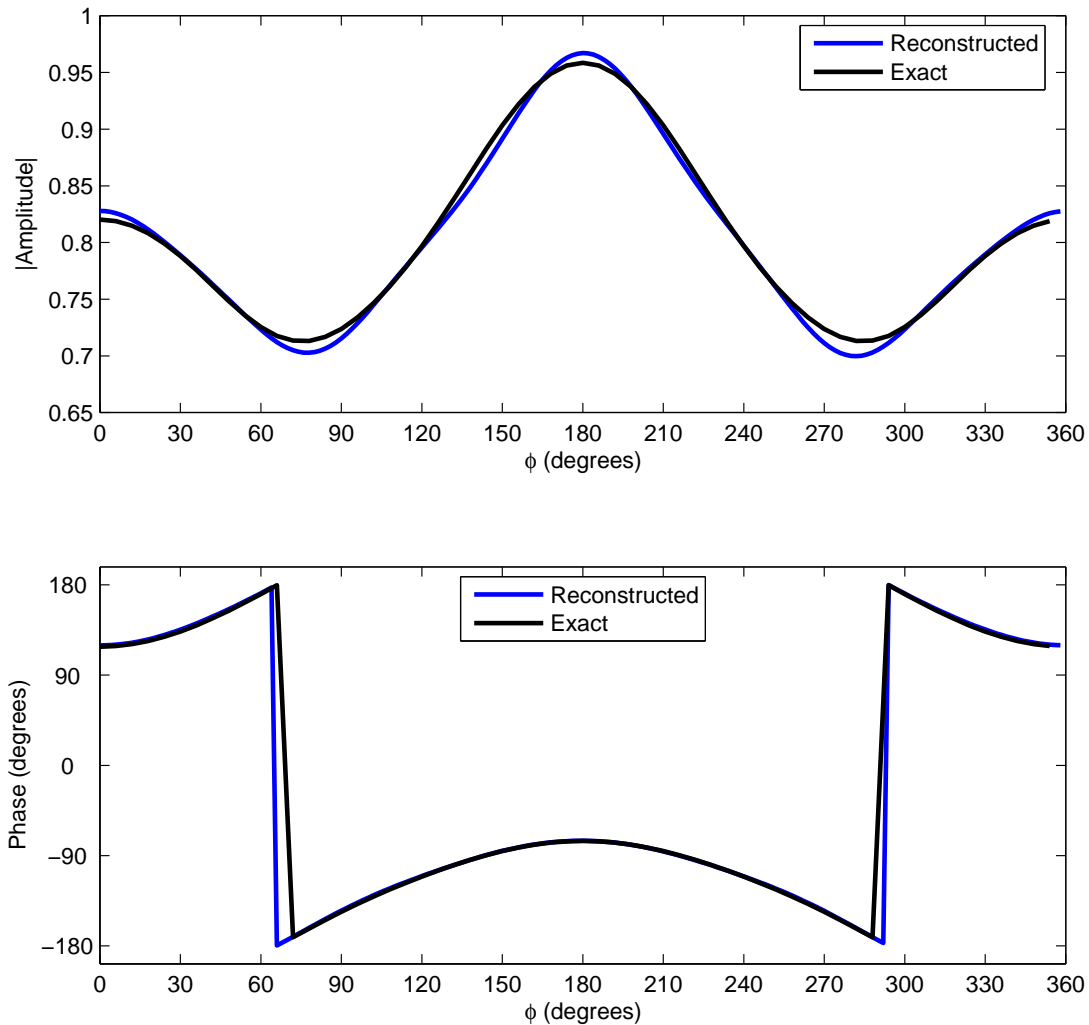
Figure 5.11: Comparison between the exact scattered field and the reconstructed scattered field calculated through the equivalent surface impedance $\eta(\phi)$ on a circle with radius $\rho = 0.3\lambda$.
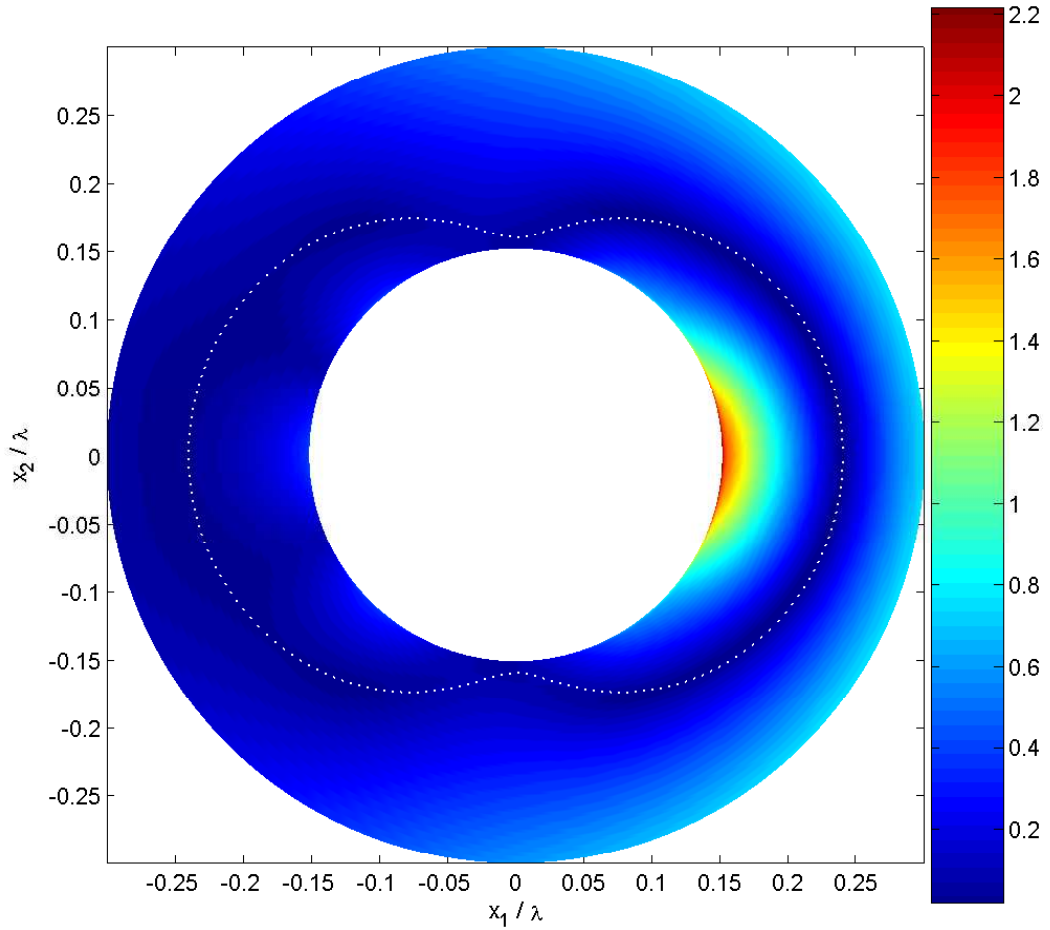
Figure 5.12: 2D variation of the amplitude of total field outside of the equivalent impedance cylinder.

may be used to choose a better initial guess for the non linear inversion. Nevertheless, being interested in assessing the performance of the method as it is, this approach is not considered in this thesis. By exploiting the reconstructed impedance and taking a circular cylinder with radius $f_0 = 0.25\lambda$ as initial guess, the shape obtained through the proposed method is shown in figure 5.13. As it can be observed, it yields to a very accurate reconstruction and the quality of the reconstruction is comparable to the previous method. The parameters adopted in the inversion are $R = 8$ and $P = 9$.

As a second example, the object given in (5.8) is considered. Here the aim is to reveal the performance of the object with a concave shape. The comparisons of the reconstructed shapes and the exact shapes are shown in figure 5.14(a), figure 5.14(b) and figure 5.14(c) for incidence angles $\theta_1 = 0$, $\theta_2 = \frac{\pi}{2}$ and $\theta_3 = \pi$ respectively. Here the simulation parameters are $\gamma = 0.36\lambda, f_0 = 0.48\lambda, P = 9$ and the regularization parameter $R = 12$ for the simulations with incidence angles θ_1, θ_3 and $R = 13$ for
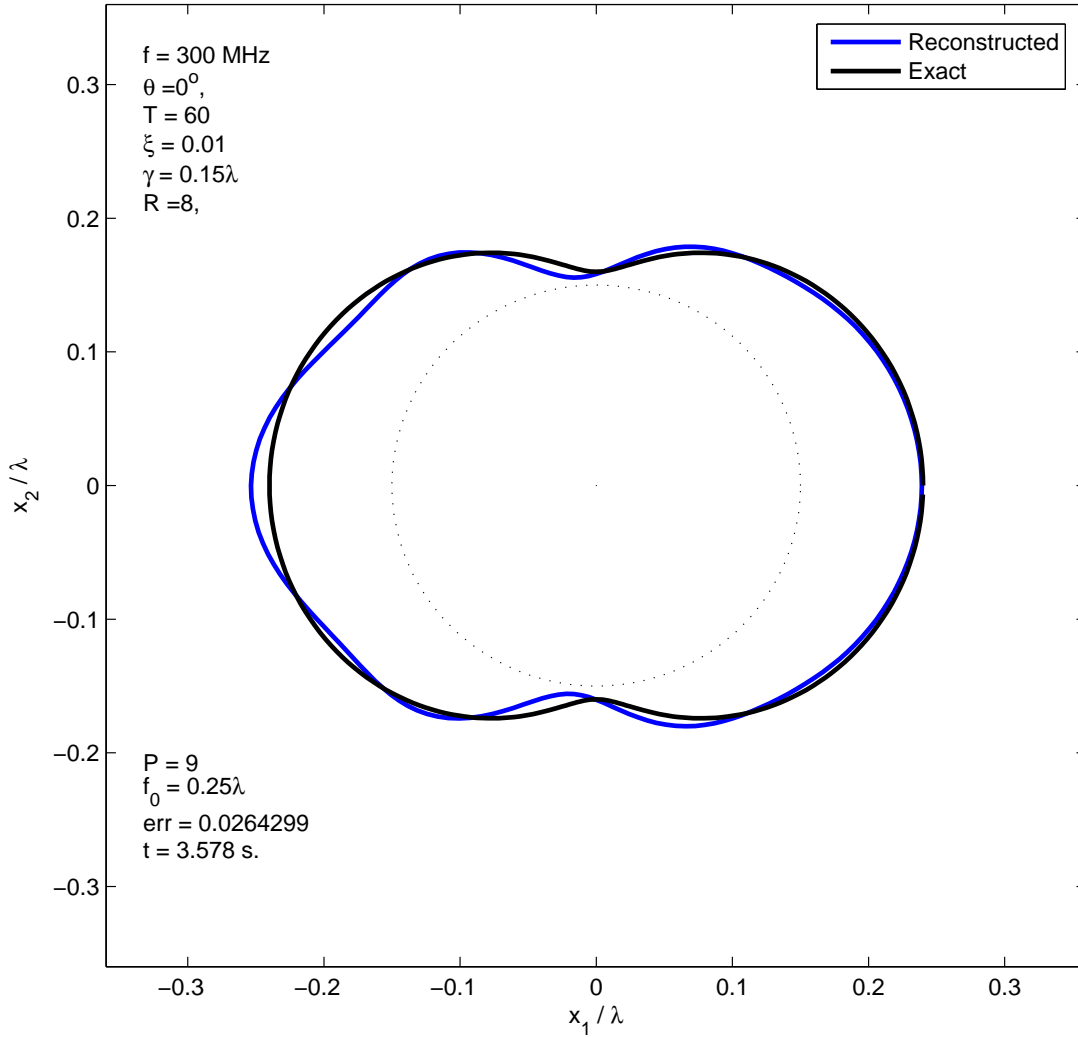
Figure 5.13: Comparison of the exact and the reconstructed shapes of the object given by the boundary ∂D_1 with a single illumination.

the simulation with $\theta_2 = \frac{\pi}{2}$. From these three figures, a similar performance has been observed as compared to previous method. The method achieves better quality at the illuminated side however quality gets worse at the unilluminated side. Later multiview simulations are performed and the comparisons of the reconstructed shapes and the exact shape are shown in figure 5.14(d) corresponding to illuminations θ_1, θ_3 and in figure 5.14(e) for the illuminations θ_2, θ_4 and finally for the illuminations $\theta_1, \theta_2, \theta_3, \theta_4$ in figure 5.14(f). Similar to the first method, the method achieved better reconstructions when more than one illumination is employed. Although overall quality of the reconstructions is quite similar to the first method, the reconstructions have more ripples in the convex part. Finally it is concluded that the diversity of illuminations are crucial on the accuracy of the reconstructions for both methods but the quality does not improve linearly with each additional illuminations.
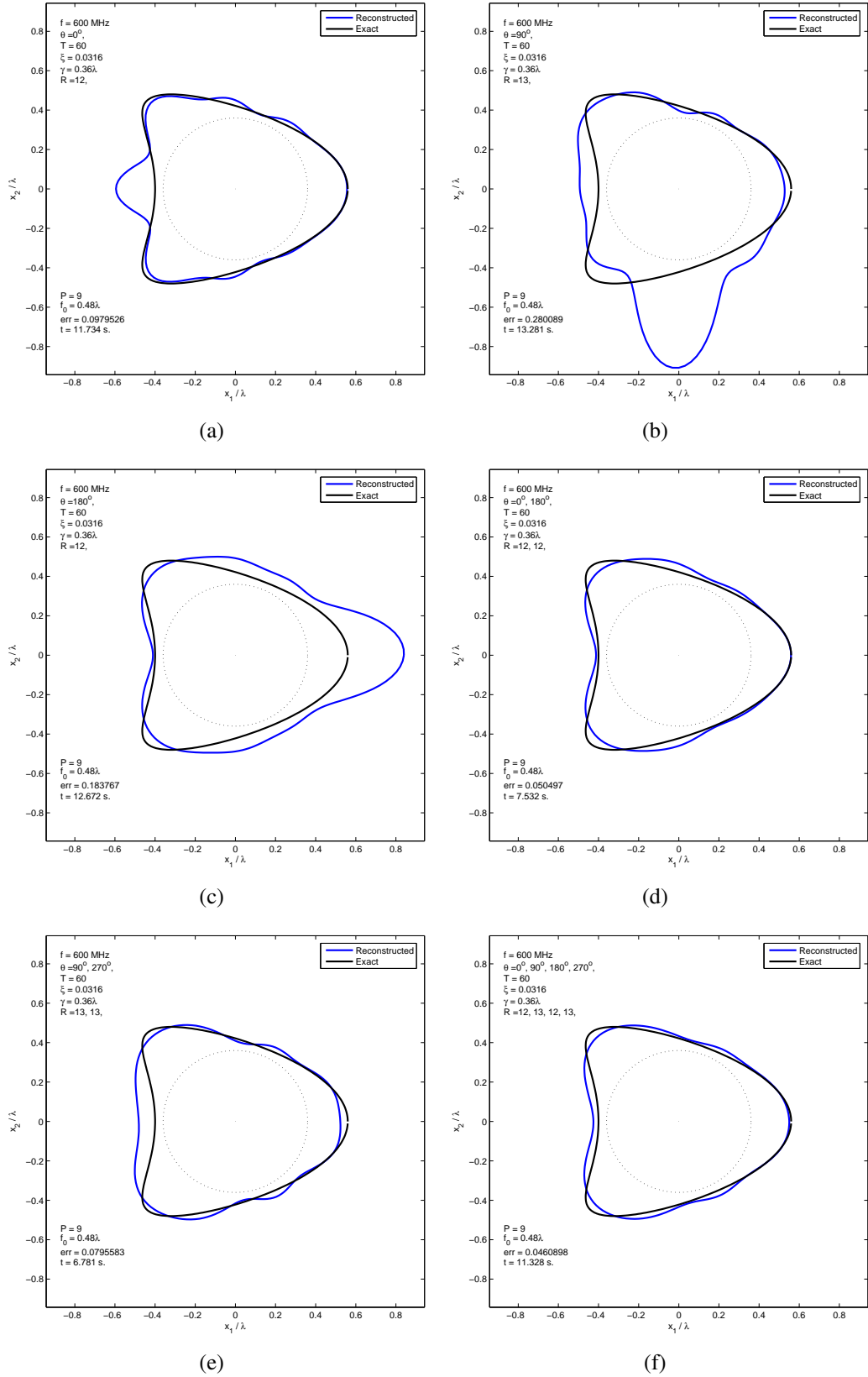
Figure 5.14: Comparison of the exact and the reconstructed shapes of the object with the boundary ∂D_2 for different incidence directions $\theta_1 = 0, \theta_2 = \frac{\pi}{2}, \theta_3 = \pi$ and $\theta_4 = \frac{3\pi}{2}$. (a) θ_1, (b) θ_2, (c) θ_3, (d) θ_1 and θ_3 (e) θ_2 and θ_4 (f) $\theta_1, \theta_2, \theta_3$ and θ_4
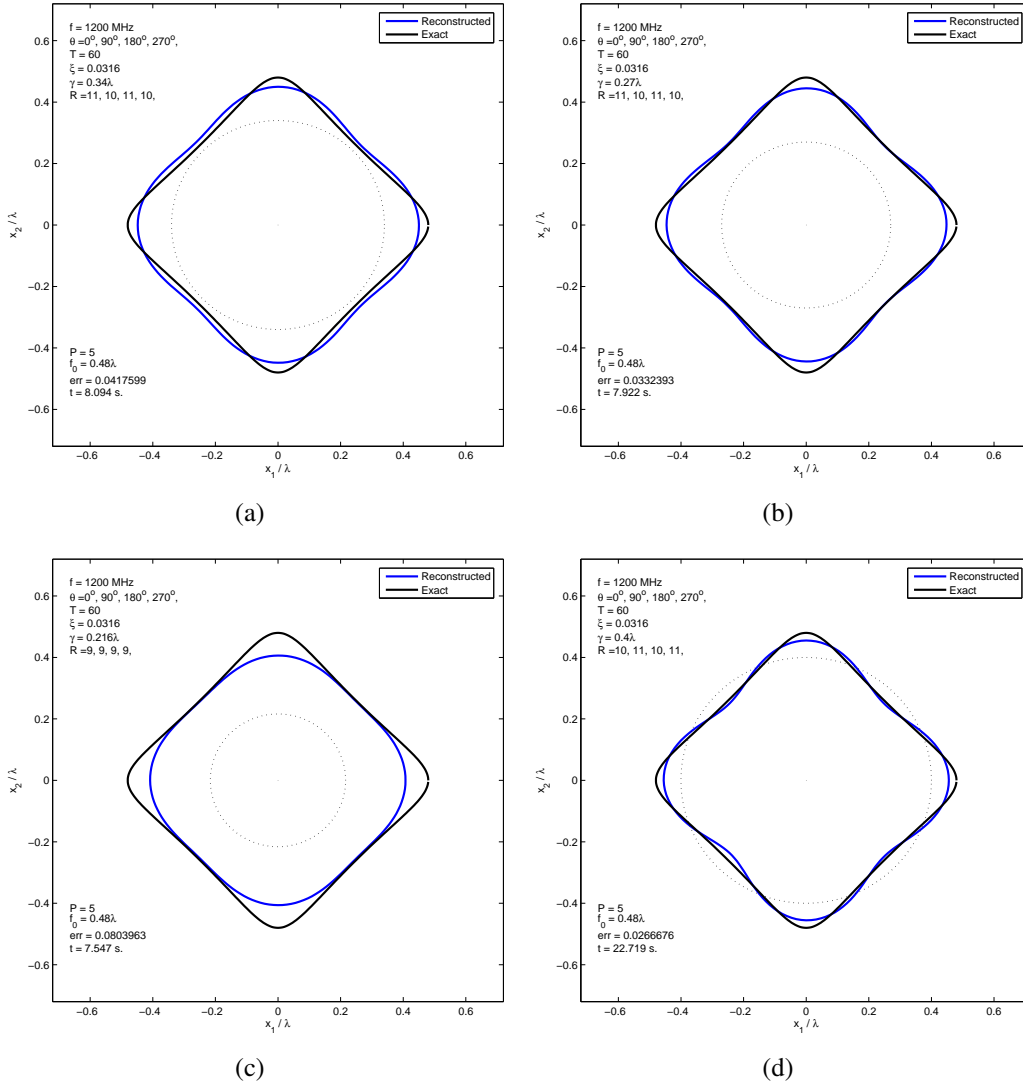
Figure 5.15: Comparison of the exact and reconstructed shapes of the object with the boundary ∂D_3 for different selection of the radius of the equivalent impedance circle. (a) $\gamma = 0.34\lambda$ (b) $\gamma = 0.27\lambda$ (c) $\gamma = 0.216\lambda$ (d) $\gamma = 0.4\lambda$

In the first method selection of the minimum circle covering the object affects the quality of reconstructions. Analogously for the second method selection of the radius of impedance circle is effective on the quality of the method. Thus here the effects of selection of the radius of the impedance circle are investigated by performing the simulation with same parameters but with different radius of impedance circles. To this aim the object whose boundary given by (5.9) is considered and simulation parameters are chosen as $P = 0, f_0 = 0.48\lambda$. The comparison between the reconstructed shape and the exact shape is shown in figure 5.15(a) when the radius $\gamma = 0.48\lambda$ which is the inner circle with maximum radius. Later the simulations are performed for the radius $\gamma = 0.27\lambda$ and the reconstructed shape is shown in figure 5.15(b). As it is clear the quality

of the reconstruction is similar to the previous simulation. The same simulation is repeated for a smaller $\gamma = 0.216\lambda$ in figure 5.15(c). Although the reconstruction is still acceptable the quality reduces as the radius of the impedance cylinder becomes smaller. Finally the reconstruction becomes completely useless for very small radii as nonlinear equation does not converge to the boundary due to increasing distance between the surface and impedance cylinder in terms of wavelength. The last simulation for this example is performed for $\gamma = 0.4\lambda$ when the impedance cylinder intersects with the unknown surface. It should be clear that there is no theoretical justification in this situation as the surface impedance is not applicable to represent the field inside but it is still interesting to see the behavior of numerical scheme when the impedance cylinder selected wrongly. The resulting reconstruction is shown in figure 5.15(d). However
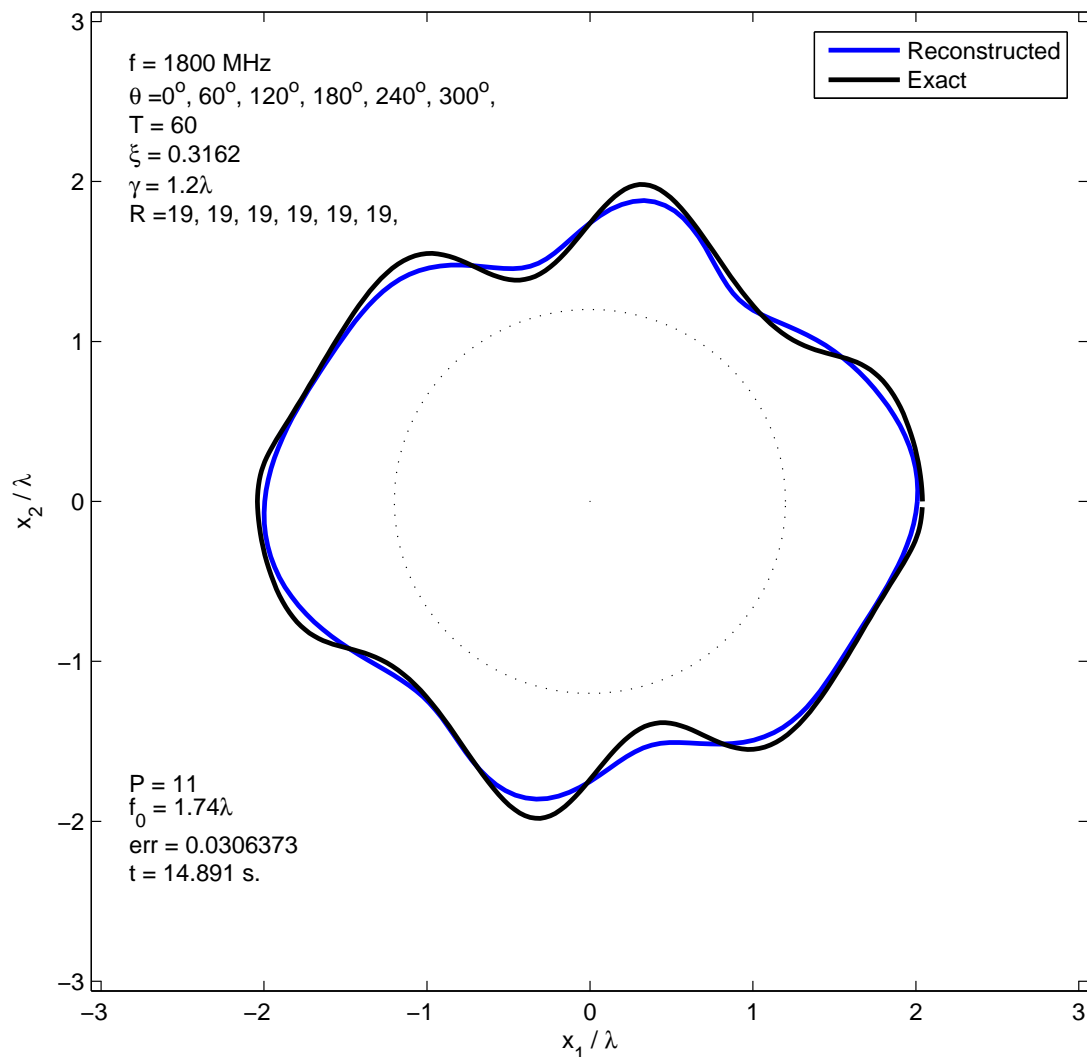
Figure 5.16: Comparison of the exact and reconstructed shapes of the object given by the boundary ∂D_4.

when the impedance cylinder completely covers the object, as expected there is no solution. The reconstruction in figure 5.15(d) is interpreted as that the method can tolerate small intersections between the target and the equivalent impedance cylinder. Finally the last example is devoted to demonstrated behavior of the method for object which are large in terms of wavelength. The object given in (5.10) is considered and simulation parameters are $P = 11, f_0 = 1.74\lambda$ and $\gamma = 1.2\lambda$. The reconstruction is shown in figure 5.16 which is a better reconstruction than the reconstruction shown in figure 5.9.

5.3 Comparison of the Shape Reconstruction Methods

In previous two sections, both methods are tested with same noisy far field patterns at each simulations to make a direct comparisons of the methods in the sense of accuracy and computation times. In table 5.1 the achieved results are summarized. Here err_1 and err_2 denote the associated reconstruction errors given by (5.1) while t_1 and t_2

Table 5.1: Comparison of the methods in terms of reconstruction errors and simulation times.

Boundary	Frequency (MHz)	Incidence angle(s) (rad)	err_1 (%)	t_1 (s.)	err_2 (%)	t_2 (s.)
∂D_1	300	0	3.023	0.70	2.642	3.58
∂D_2	600	0	13.139	2.09	9.795	11.73
∂D_2	600	$\frac{\pi}{2}$	15.362	2.24	28.008	13.28
∂D_2	600	π	17.578	2.05	18.376	12.67
∂D_2	600	$0, \pi$	4.707	2.50	5.049	7.53
∂D_2	1200	$\frac{\pi}{2}, \frac{3\pi}{2}$	7.451	2.45	7.955	6.78
∂D_2	1200	$0, \frac{\pi}{2}, \pi, \frac{3\pi}{2}$	5.564	3.06	4.608	11.33
∂D_3	1200	$0, \frac{\pi}{2}, \pi, \frac{3\pi}{2}$	3.404	3.92	4.175	8.09
∂D_3	1200	$0, \frac{\pi}{2}, \pi, \frac{3\pi}{2}$	2.793	5.20	3.323	7.92
∂D_3	1200	$0, \frac{\pi}{2}, \pi, \frac{3\pi}{2}$	3.777	4.81	8.039	7.55
∂D_3	1200	$0, \frac{\pi}{2}, \pi, \frac{3\pi}{2}$	4.195	4.19	2.666	22.72
∂D_4	1800	$0, \frac{\pi}{3}, \frac{2\pi}{3}, \pi, \frac{4\pi}{3}, \frac{5\pi}{3}$	5.787	4.86	3.063	14.89

shows the simulation times in seconds for the Taylor series based method and surface impedance modeling based method, respectively. As it can be concluded from the results, both methods provide similar reconstructions, thus there is no preference over the methods in the sense of accuracy. However it is clear that the surface impedance modeling based method is slower then Taylor series based method in all cases. This is due to the fact that the second method requires to solve forward problem as compared to the first method which does not. Although this may be seen as a drawback, it should be noted that in any case simulations generally took less than 20s. on a regular PC. Thus both methods are quite fast as compared to sampling based methods and other iterative methods. Another important conclusion is that introduction of Gauss-Newton algorithm for multiview data increased the quality of reconstructions while adding less computational effort.

6. CONCLUSIONS

Inverse scattering problems whose aim is to retrieve the requested physical properties of inaccessible objects appear in many areas of engineering and applied sciences. Within this framework, the shape reconstruction problem for inaccessible, perfect electric conducting targets is studied in this thesis. Consequently, two different shape reconstruction methods which can be considered in the class of analytical continuation methods are developed. Both methods handle the ill-posedness and the nonlinearity of the underlying inverse scattering problem separately. These methods are numerically validated through the simulations and certain capabilities and limitations of the methods are demonstrated.

Both of the presented methods provide quite accurate reconstructions for objects having starlike boundaries with convex and concave parts. With an identical configuration, the simulation results for the each method are comparable, thus there is no preference over methods in terms of accuracy. It is observed that accuracy of both methods improves when the variation of the boundary is slow. Both methods produce better reconstructions at illuminated part of the object. When a single illumination at a fixed frequency is employed, it is observed that the size of the object should be comparable or smaller than the wavelength for both methods to get satisfactory reconstructions. This limitation regarding to the size of targets is improved by extending the methods via Gauss - Newton algorithm so that both methods can exploit all the available far field data simultaneously when multiple illuminations are used. With the introduction of multiview data, both methods can reconstruct objects larger than wavelength and the robustness against noise is increased which means that the methods are capable of reconstructing objects of larger size with data having low SNR. Even in the multiview configuration only a few illuminations are enough as long as the diversity of incidence angles are not in a limited aperture. As a result the data requirement is quite low as compared to sampling based methods such as linear sampling which is not a viable as long as the target is illuminated in many directions.

Selection of regularization parameter greatly affects the quality of reconstructions. Since both methods handles ill-posedness of the problem in a single step, only one regularization parameter is required. This simplicity is an important advantage over other optimization based reconstruction methods which require choosing a regularization parameter at each iteration.

The computational requirements of the method based of Taylor series representation of the scattered field are lower than the method based on inhomogeneous surface impedance modeling since the latter requires to solve the associated the direct scattering problem as a part of reconstruction algorithm. But still both methods perform generally less than 20s with a regular PC configuration.

Although the shape reconstruction methods are presented in the context of electromagnetic waves, these methods are valid for acoustical waves with sound soft obstacles as well. The future research will focus on extending the methods to 3D problems of electromagnetic and acoustical waves.

REFERENCES

[1] **Kirsch, A.**, 1996. *An Introduction to the Mathematical Theory of Inverse Problems*, Springer New York.

[2] **Colton, D. and Kress, R.**, 1998. *Inverse Acoustic and Electromagnetic Scattering Theory*, Springer-Verlag, 2nd ed. edition.

[3] **Imbriale, W. and Mittra, R.**, 1970. The two-dimensional inverse scattering problem, *Antennas and Propagation, IEEE Transactions on [legacy, pre - 1988]*, **18(5)**, 633–642.

[4] **Colton, D.**, 1981. The inverse electromagnetic scattering problem for a perfectly conducting cylinder, *Antennas and Propagation, IEEE Transactions on*, **29(2)**, 364–368.

[5] **Bojarski, N.**, 1982. A survey of the physical optics inverse scattering identity, *IEEE Trans. Antennas Propag.*, **30(5)**, 980–989.

[6] **Pierri, R.**, **Liseno, A. and Soldovieri, F.**, 2001. Shape reconstruction from PO multifrequency scattered fields via the singular value decomposition approach, *IEEE Trans. Antennas Propag.*, **49(9)**, 1333–1343.

[7] **Soldovieri, F.**, **Brancaccio, A.**, **Leone, G. and Pierri, R.**, 2005. Shape reconstruction of perfectly conducting objects by multiview experimental data, *Geoscience and Remote Sensing, IEEE Transactions on*, **43(1)**, 65–71.

[8] **Roger, A.**, 1981. Newton-Kantorovitch algorithm applied to an electromagnetic inverse problem, *Antennas and Propagation, IEEE Transactions on [legacy, pre - 1988]*, **29(2)**, 232–238.

[9] **Lin, C.Y. and Kiang, Y.W.**, 1996. Inverse scattering for conductors by the equivalent source method, *IEEE Trans. Antennas Propag.*, **44(3)**, 310–316.

[10] **Kirsch, A. and Kress, R.**, 1987. An optimization method in inverse acoustic scattering, **B. et al**, editor, Boundary elements IX, Vol 3. Fluid Flow and Potential Applications, Springer-Verlag, Berlin.

[11] **Kress, R.**, 2003. Newton's method for inverse obstacle scattering meets the method of least squares, *Inverse Problems*, **19(6)**, S91–S104, *<http://stacks.iop.org/0266-5611/19/S91>*.

[12] **Serranho, P.**, 2006. A hybrid method for inverse scattering for shape and impedance, *Inverse Problems*, **22(2)**, 663–680, *<http://stacks.iop.org/0266-5611/22/663>*.

[13] **Çayören, M.**, **Akduman, I.**, **Yapar, A. and Crocco, L.**, 2007. A new algorithm for the shape reconstruction of perfectly conducting objects, *Inverse Problems*, **23(3)**, 1087–1100, *<http://stacks.iop.org/0266-5611/23/1087>*.

[14] **Çayören, M.**, **Akduman, I.**, **Yapar, A. and Crocco, L.**, 2008. Shape Reconstruction of Perfectly Conducting Targets From Single-Frequency Multiview Data, *IEEE Geosci. Remote Sens. Lett.*, **5(3)**, 383–386.

[15] **Çayören, M.**, **Akduman, I.**, **Yapar, A. and Crocco, L.**, 2009. Surface impedance modeling of PEC targets: application to shape reconstruction, *Inverse Problems*, (in press).

[16] **Colton, D. and Kirsch, A.**, 1996. A simple method for solving inverse scattering problems in the resonance region, *Inverse Problems*, **12(4)**, 383–393, *<http://stacks.iop.org/0266-5611/12/383>*.

[17] **Colton, D.**, **Piana, M. and Potthast, R.**, 1997. A simple method using Morozov's discrepancy principle for solving inverse scattering problems, *Inverse Problems*, **13(6)**, 1477–1493, *<http://stacks.iop.org/0266-5611/13/1477>*.

[18] **Colton, D.**, **Coyle, J. and Monk, P.**, 2000. Recent Developments in Inverse Acoustic Scattering Theory, *SIAM Review*, **42(3)**, 369–414, *<http://link.aip.org/link/?SIR/42/369/1>*.

[19] **Colton, D.**, **Haddar, H. and Piana, M.**, 2003. The linear sampling method in inverse electromagnetic scattering theory, *Inverse Problems*, **19(6)**, S105–S137, *<http://stacks.iop.org/0266-5611/19/S105>*.

[20] **Cakoni, F. and Colton, D.**, 2006. *Qualitative Methods in Inverse Scattering Theory*, Springer.

[21] **Catapano, I.**, **Crocco, L. and Isernia, T.**, 2007. On Simple Methods for Shape Reconstruction of Unknown Scatterers, *IEEE Trans. Antennas Propag.*, **55(5)**, 1431–1436.

[22] **Kirsch, A.**, 1998. Characterization of the shape of a scattering obstacle using the spectral data of the far field operator, *Inverse Problems*, **14(6)**, 1489–1512, *<http://stacks.iop.org/0266-5611/14/1489>*.

[23] **Kirsch, A. and Grinberg, N.**, 2008. *The Factorization Method for Inverse Problems*, Oxford University Press.

[24] **Ikehata, M.**, 1998. Reconstruction of an obstacle from the scattering amplitude at a fixed frequency, *Inverse Problems*, **14(4)**, 949–954, *<http://stacks.iop.org/0266-5611/14/949>*.

[25] **Potthast, R.**, 2001. *Point Sources and Multipoles in Inverse Scattering Theory*, Chapman & Hall/CRC.

[26] **Potthast, R.**, 2006. A survey on sampling and probe methods for inverse problems, *Inverse Problems*, **22(2)**, R1–R47, *<http://stacks.iop.org/0266-5611/22/R1>*.

[27] **Luke, D.R. and Potthast, R.**, 2003. The No Response Test—A Sampling Method for Inverse Scattering Problems, *SIAM Journal on Applied Mathematics*, **63(4)**, 1292–1312, *<http://link.aip.org/link/?SMM/63/1292/1>*.

[28] **Potthast, R.**, **Sylvester, J. and Kusiak, S.**, 2003. A range test for determining scatterers with unknown physical properties, *Inverse Problems*, **19(3)**, 533–547, *<http://stacks.iop.org/0266-5611/19/533>*.

[29] **Dorn, O. and Lesselier, D.**, 2006. Level set methods for inverse scattering, *Inverse Problems*, **22(4)**, R67–R131, *<http://stacks.iop.org/0266-5611/22/R67>*.

[30] **Qing, A.**, **Lee, C.K. and Jen, L.**, 2001. Electromagnetic inverse scattering of two-dimensional perfectly conducting objects by real-coded genetic algorithm, *IEEE Trans. Geosci. Remote Sens.*, **39(3)**, 665–676.

[31] **Rekanos, I.T.**, 2008. Shape Reconstruction of a Perfectly Conducting Scatterer Using Differential Evolution and Particle Swarm Optimization, *IEEE Trans. Geosci. Remote Sens.*, **46(7)**, 1967–1974.

[32] **Kirsch, A.**, 2004. The factorization method for Maxwell's equations, *Inverse Problems*, **20(6)**, S117–S134, *<http://stacks.iop.org/0266-5611/20/S117>*.

[33] **Colton, D. and Kress, R.**, 1992. *Integral Equation Methods in Scattering Theory*, Krieger Pub. Malabar Florida.

[34] **Abramowitz, M. and Stegun, I.A.**, 1964. Handbook of Mathematical Functions with Formulas, Graphs, and Mathematical Tables, Dover, New York, ninth dover printing, tenth gpo printing edition.

[35] **Bertero, M.**, 1989. *Linear inverse and ill-posed problems. In Advances in Electronics and Electron physics*, Academic Press, New York.

[36] **Bucci, O.M. and Isernia, T.**, 1997. Electromagnetic inverse scattering: Retrievable information and measurement strategies, *Radio Sci.*, **32(6)**, 2123–2137.

[37] **Morozov, V.**, 1984. *Methods for Solving Incorrectly Posed Problems*, Springer-Verlag.

[38] **Bucci, O.M.**, **Crocco, L. and Isernia, T.**, 1999. Improving the reconstruction capabilities in inverse scattering problems by exploitation of close-proximity setups, *J. Opt. Soc. Am. A*, **16(7)**, 1788–1798, *<http://josaa.osa.org/abstract.cfm?URI=josaa-16-7-1788>*.

[39] **Yapar, A.**, **Ozdemir, O.**, **Sahinturk, H. and Akduman, I.**, 2006. A Newton method for the reconstruction of perfectly conducting slightly rough surface profiles, *IEEE Trans. Antennas Propag.*, **54(1)**, 275–279.

[40] **Akduman, I.**, **Kress, R. and Yapar, A.**, 2006. Iterative reconstruction of dielectric rough surface profiles at fixed frequency, *Inverse Problems*, **22(3)**, 939–954, *<http://stacks.iop.org/0266-5611/22/939>*.

[41] **İbrahim Akduman**, **Çayören, M.**, **Yapar, A. and Crocco, L.**, 2007. Resolution Improvement of Analytical Continuation Method by Multiview Data, Proc. 8th International Conference on Mathematical and Numerical Aspects of Waves.

[42] **Chong, E.K.P. and Zak, S.H.**, 2001. *An Introduction to Optimization*, John Wiley & Sons, 2nd. edition.

[43] **Hoppe, D. and Rahmat-Samii, Y.**, 1995. *Impedance Boundary Conditions In Electromagnetics*, Taylor & Francis.

[44] **Senior, T.B.A. and Volakis, J.L.**, 1995. *Approximate Boundary Conditions In Electromagnetics*, IEE Press, New York and London.

[45] **Marceaux, O. and Stupfel, B.**, 2000. High-order impedance boundary conditions for multilayer coated 3-D objects, *IEEE Trans. Antennas Propag.*, **48(3)**, 429–436.

[46] **Ozdemir, O.**, **Akduman, I.**, **Yapar, A. and Crocco, L.**, 2007. Higher Order Inhomogeneous Impedance Boundary Conditions for Perfectly Conducting Objects, *IEEE Trans. Geosci. Remote Sens.*, **45(5)**, 1291–1297.

[47] **Akduman, I. and Yapar, A.**, 2001. Surface impedance determination of a planar boundary by the use of scattering data, *IEEE Trans. Antennas Propag.*, **49(2)**, 304–307.

[48] **Akduman, I. and Kress, R.**, 2003. Direct and inverse scattering problems for inhomogeneous impedance cylinders of arbitrary shape, *Radio Sci.*, **Vol 38, No 3**, 1055.

[49] **Colton, D. and Cakoni, F.**, 2004. The Determination of the Surface Impedance of a Partially Coated Obstacle from Far Field Data, *SIAM Journal on Applied Mathematics*, **64(2)**, 709–723.

[50] **Leontovich, M.**, 1948. *Investigations of Radio Wave Propagation, Part II*, Academy of Sciences, USSR, Moscow.

[51] **Sahinturk, H.**, 2004. On the reconstruction of inhomogeneous surface impedance of cylindrical bodies, *IEEE Trans. Magn.*, **40(2, Part 2)**, 1152–1155.

[52] **Kress, R.**, 1995. On the Numerical Solution of a Hypersingular Integral Equation in Scattering Theory, *Journal of Computational and Applied Mathematics*, **Volume 61, Issue 3**, 345–360.

[53] **Kress, R.**, 1999. *Linear Integral Equations*, Springer New York, 2nd. edition.

[54] **Engl, H.W. and Grever, W.**, 1994. Using the L-curve for determining optimal regularization parameters, *Numerische Mathematik*, **69(1)**, 25–31.

[55] **Bucci, O.M.**, **Capozzoli, A. and D'Elia, G.**, 2002. Determination of the convex hull of radiating or scattering systems: a new, simple and effective approach, *Inverse Problems*, **18(6)**, 1621–1638, *<http://stacks.iop.org/0266-5611/18/1621>*.

[56] **Crocco, L.**, **D'Urso, M. and Isernia, T.**, 2005. Testing the contrast source extended Born inversion method against real data: the TM case, *Inverse Problems*, **21(6)**, S33–S50, *<http://stacks.iop.org/0266-5611/21/S33>*.

[57] **Kress, R.**, 1998. *Numerical Analysis*, Springer New York.

APPENDICES

APPENDIX A : NUMERICAL EVALUATION OF TSVD INVERSION

APPENDIX B : REDUCTION OF SIBC TO SCALAR CASE

A. NUMERICAL EVALUATION OF TSVD INVERSION

The theoretical background of the TSVD inversion is discussed in section 3.1. As both of the presented shape reconstruction methods require the integral equation

$$u^\infty(\phi) = \frac{e^{i\pi/4}}{\sqrt{8\pi k}} \int_0^{2\pi} e^{-ik\cos(\phi-\tau)} \Psi(\tau)\alpha \mathrm{d}\tau \tag{A.1}$$

to be inverted to solve the unknown single-layer potential density Ψ, here numerical aspects of the TSVD inversion are addressed.

The far field pattern is only known at total T discreet measurements points, thus (A.1) is reduced to a system of linear equation. The integral appearing in (A.1) is approximated with trapezoidal rule

$$\int_0^{2\pi} f(\tau)\mathrm{d}\tau \cong \frac{2\pi}{L} \sum_{\ell=0}^{L-1} f(\ell\frac{2\pi}{L}). \tag{A.2}$$

It is possible to use different quadrature rules, however the trapezoidal rule is intentionally selected because of its simplicity and its fast convergence for this kind of integrals [57]. The resulting system of linear equations is in the form of

$$S\Psi = u^\infty \tag{A.3}$$

where S is an $T \times L$ matrix of whose elements $s_{t,\ell}$ are given by

$$s_{t,l} = \sqrt{\frac{i\pi}{2k}} \frac{\alpha}{L} e^{-ik\cos(\phi_t - \tau_\ell)}, \quad \phi_t = t\frac{2\pi}{T}, \ \tau_l = l\frac{2\pi}{L} \tag{A.4}$$

and column vectors Ψ and u^∞ given accordingly

$$\Psi = [\Psi_1, \Psi_2, \cdots, \Psi_L]^T, \quad \Psi_l = \Psi(\tau_\ell) \tag{A.5}$$

and

$$u^\infty = [u_1^\infty, u_2^\infty, \cdots, u_T^\infty]^T, \quad u_t^\infty = u^\infty(\phi_t). \tag{A.6}$$

The SVD of (A.3) consist of three matrices

$$S = U\Sigma V^* \tag{A.7}$$

where U and V are unitary matrices and Σ is a diagonal matrix

$$\Sigma = diag(\sigma_1, \sigma_2, \ldots, \sigma_P), \quad P = \min(L, T), \ \sigma_1 > \sigma_2, \ldots, \sigma_P. \tag{A.8}$$

which contains the singular values σ_p in decreasing order and $\sigma_1 = ||S||$. Since U and V are unitary matrices, (A.7) provides the following generalized inversion formula

$$S^{-1} = V\Sigma^+ U^* \tag{A.9}$$

where

$$\Sigma^+ = diag\left(\frac{1}{\sigma_1}, \frac{1}{\sigma_2}, \dots, \frac{1}{\sigma_P}\right). \tag{A.10}$$

As explained above (A.9) provides a convenient formula to solve unknown Ψ. However as a result of ill-posedness of the integral equation in (A.1), the linear system (A.3) turns out to be ill-conditioned which is defined as the ratio of maximum singular value to minimum singular value $\kappa = \frac{\sigma_{max}}{\sigma_{min}}$, to be very large. Inversion of the ill-conditioned linear system (A.3) leads to instabilities which means small perturbations on u^∞ cause extremely large variations in Ψ. Moreover the noise on u^∞ completely overwhelms higher order singular values as their values are lower than the noise level thus their inclusion in the calculations increases the instability. Consequently, by omitting the higher order singular values and their corresponding vectors, it is possible to achieve a better conditioned linear system

$$\Psi^{(R)} = \tilde{V}^* \tilde{\Sigma}^+ \tilde{U} u^\infty \tag{A.11}$$

which has a same matrix norm with the original system. Here R denotes the regularization parameter which is actually the total number of significant singular values and $\tilde{V}^*, \tilde{\Sigma}^+, \tilde{U}$ correspond the truncated versions of associated matrices. Now the issue becomes how to select which singular values are significant. To this aim it is possible to use Morozov's discrepancy principle which requires to calculate (3.6) with an increasing number of R until it satisfies the condition in (3.7).

B. REDUCTION OF SIBC TO SCALAR CASE

The standard impedance boundary condition is given by

$$-\hat{\mathbf{n}} \times (\hat{\mathbf{n}} \times \mathbf{E}) = Z\hat{\mathbf{n}} \times \mathbf{H}. \tag{B.1}$$

where $\mathbf{E}$ and $\mathbf{H}$ are respectively the total electric field and magnetic field vectors on a given boundary on which the surface impedance Z and the outward unit normal vector $\hat{\mathbf{n}}$ are defined [43, 44]. $\mathbf{E}$ is polarized towards Ox_3 direction in the problem configuration described in section 2.1

$$\mathbf{E} = u\hat{x}_3. \tag{B.2}$$

Substituting (B.2) together with Faraday's Law for the time harmonic case

$$\nabla \times \mathbf{E} = -i\omega\mu\mathbf{H} \tag{B.3}$$

into (B.1) results the following equation after straightforward calculations

$$u\hat{x}_3 = -i\frac{Z}{\omega\mu}\hat{n} \times (\nabla \times \mathbf{E}). \tag{B.4}$$

The right hand side of (B.4) is simplified as

$$\hat{n} \times (\nabla \times u\hat{x}_3) = -(\hat{n}.\nabla)u\hat{x}_3 = -\frac{\partial u}{\partial n}\hat{x}_3 \tag{B.5}$$

by using the following vector calculus identity

$$\mathbf{A} \times (\nabla \times \mathbf{B}) = \nabla_B(\mathbf{A} \times \mathbf{B}) - (\mathbf{A}.\nabla)\mathbf{B} \tag{B.6}$$

where ∇_B means the gradient operates on only $\mathbf{B}$. The resulting equation

$$u\hat{x}_3 - i\frac{Z}{\omega\mu}\frac{\partial u}{\partial n} = 0 \tag{B.7}$$

Consequently, by combining

$$k = \omega\sqrt{\varepsilon'\mu} \tag{B.8}$$

$$Z_0 = \sqrt{\frac{\mu}{\varepsilon'}} \tag{B.9}$$

and

$$\eta = \frac{Z}{Z_0} \tag{B.10}$$

into (B.7) gives the the final equation after straightforward arrangements

$$\frac{\partial u}{\partial n}(\mathbf{x}) + \frac{ik}{\eta(\mathbf{x})}u(\mathbf{x}) = 0. \tag{B.11}$$

CURRICULUM VITAE

Candidate's full name:
Mehmet ÇAYÖREN

Place and date of birth:
Sivas, 1979

Permanent Address:
Tufan Mh. Akgüngör Sk. No:9/2, 34688 Üsküdar, İstanbul, Turkey.

Universities and Colleges attended:

2004 -	:	Ph.D. Candidate in Electronics and Communication Engineering Istanbul Technical University, Turkey.
2002 - 2004	:	M.Sc. in Electronics and Communication Engineering Istanbul Technical University, Turkey.
1997 - 2001	:	B.Sc. in Electrical and Electronics Engineering Istanbul University, Turkey.
2007 - 2008		Visiting researcher in Mathematical Sciences Dept. University of Delaware, USA.

Publications:

- Kılıç E., **Çayören M.**, Yapar A., Akduman I. 2009. Reconstruction of Perfectly Conducting Rough Surfaces by the Use of Inhomogeneous Surface Impedance Modeling *Inverse Problems and Imaging*, **3(2)**.

- Cakoni F., **Çayören M.**, and Colton D. 2008. Transmission Eigenvalues and the Nondestructive Testing of Dielectrics, *Inverse Problems*, **24(6)**.

- **Çayören M.**, Akduman, I., Yapar, A. and Crocco, L., 2008. Shape Reconstruction of Perfectly Conducting Targets From Single-Frequency Multiview Data, *IEEE Geosci. Remote Sens. Lett.*, **5(3)**, 383–386.

- **Çayören M.**, Akduman, I., Yapar, A. and Crocco, L., 2007. A New Algorithm for the Shape Reconstruction of Perfectly Conducting Objects, *Inverse Problems*, **23(3)**, 1087–1100.

Conference Proceedings:

- Ünal G. S., **Çayören M.**, and Tetik E., 2008. Reconstruction of Surface Impedance of an Object Located over a Planar PEC Surface *6th International Conference on Inverse Problems in Engineering: Theory and Practice (ICIPE)*, June 15 - 19 2008, Paris, France.

- **Çayören M.**, Şahintürk H., and Crocco L., 2008. Improving a Shape Reconstruction Method by Means of Frequency and Angle Diversity *The 23rd Progress in Electromagnetics Research Symposium (PIERS) in Hangzhou*, March 24 - 28 2008, Hangzhou, PRC.

- Akduman İ., **Çayören M.**, and Yapar A., 2008. A Method for the Shape Reconstruction of a Perfectly Conducting Object Buried in a Half-space *The 23rd Progress in Electromagnetics Research Symposium (PIERS) in Hangzhou*, March 24 - 28 2008, Hangzhou, PRC.

- Ünal G. S., **Çayören M.**, and Tetik E., 2008. Determination of Earth Surface Roughness through Surface Impedance Modeling *The 10th Specialist Meeting on Microwave Radiometry And Remote Sensing Of The Environment*, March 11 - 14 2008, Florence, Italy.

- **Çayören M.**, Özdemir Ö., and Akduman İ., 2007. The Use of Inhomogeneous Surface Impedance Modeling in the Shape Reconstruction *Progress in Electromagnetics Research Symposium (PIERS) in Prague* August 27 - 30, 2007 Prague, Czech Republic.

- Aslanyürek B., **Çayören M.**, and Şahintürk H., 2007. A Hybrid Method for the Scattering of Electromagnetic Waves from Coatings of Variable Thickness *Progress in Electromagnetics Research Symposium (PIERS) in Prague* August 27 - 30, 2007 Prague, Czech Republic.

- Akduman İ., **Çayören M.**, Yapar A., and Crocco L., 2007. Resolution Improvement of Analytical Continuation Method by Multiview Data *The 8th International Conference on Mathematical and Numerical Aspects of Waves (Waves 2007)* July 23 - 27, 2007 Reading - Berkshire, UK.

- **Çayören M.**, Akduman I., Yapar A., and Crocco L., 2007. A New Algorithm for the Shape Reconstruction of Perfectly Conducting Objects *Progress in Electromagnetics Research Symposium (PIERS) in Beijing* March 26 - 30, 2007 Beijing, PRC.

- **Çayören M.**and Aslanyürek B., 2007. A New Approach for the Scattering of Electromagnetic Waves from Dielectric Bodies of Arbitrary Shape *Progress in Electromagnetics Research Symposium (PIERS) in Beijing* March 26 - 30, 2007 Beijing, PRC.

- Crocco L., Akduman İ., **Çayören M.**, and Ali Yapar, 2007. A New Method for Shape Reconstruction of Perfectly Conducting Targets *The 23rd Annual Review of Progress in Applied Computational Electromagnetics* March 19 - 23, 2007 Verona, Italy.